Chapter 4
Wetting on Rough Surfaces

Abstract There are two possible wetting states, Wenzel and Cassie-Baxter, when liquid wets a rough surface. In the Wenzel state, liquid fully wets every area of the rough surface. For hydrophilic material, roughness enhances wettability and results in superhydrophilicity. On the other hand, roughness increases the surface's resistance to wet for moderately hydrophilic and hydrophobic material. The advancing contact line sometimes prematurely pins the liquid droplet into a metastable wetting state, resulting in an anomalously large contact angle. Vibration of the drop de-pins the contact line and relocates the droplet to an equilibrium position with a smaller equilibrium contact angle $\boldsymbol{\theta}_{\text{eq}}$. The calculated Wenzel angle agrees well with $\boldsymbol{\theta}_{\text{eq}}$ confirming that vibration leads to the most stable wetting state on the rough surface. Roughness geometry is shown to have a profound effect on the wetting and spreading process. While surface with cavities and pores wets similarly to the smooth surface, bumps on the other hand interact with the contact line, they retard contact line advancing during spread and drag the contact line during receding. In the case of the Cassie–Baxter state, pockets of air are trapped during liquid wetting, forming a liquid–solid–air composite interface. This interface is characterized by a large contact angle along with a small sliding angle. Surface texture/roughness, low surface energy material, and re-entrant geometry are key design parameters for both superhydrophobicity and superoleophobicity. Since the fully wetted Wenzel state is usually more stable, a lot of attention has been paid to stabilize the Cassie–Baxter state by increasing the energy barrier between them. Hierarchical roughness structure and re-entrant angle at the liquid–solid–air interface are shown to be key enablers, not only to stabilize the Cassie–Baxter composite state from transitioning to the Wenzel state, but also to increase its resistance to collapse when an external pressure is applied. Cassie–Baxter composite state can also be formed on groove surfaces, which will lead to directional wetting. Droplets are shown to move faster in the direction parallel to the grooves through wetting of the solid strips. This is evident by imaging the advancing contact line with a hot polyethylene wax. In the orthogonal direction, the contact line advances by hopping from one solid strip to another. This increases the chance of pinning and results in both large contact angle and sliding angle. With appropriate surface texturing, surface with interesting unidirectional spreading ability has been reported. Despite the fascinating wetting properties and its numerous application potentials, technology implementation of rough surfaces is lagged. The major hurdle for crossing the chasm between research and product is discussed.

K.-Y. Law, H. Zhao, *Surface Wetting*, DOI 10.1007/978-3-319-25214-8_4

Keywords Wetting • Rough surfaces • Wenzel equation • Cassie–Baxter equation • Wettability • Wetting dynamics • Roughness factor • Roughness geometry • Drop vibration • Metastable wetting state • Most stable wetting state • Superhydrophilicity • Antifogging • Self-cleaning • Superhydrophobicity • Wenzel Cassie–Baxter transition • Superoleophobicity • Re-entrant angle • Directional wetting • Unidirectional wetting

4.1 The Two Classic Wetting Models

The concept of wetting a rough surface was first described by Wenzel [1]. Using the thermodynamic argument, he stated that if a liquid wets a solid surface favorably, its wettability will be enhanced on the rough surface. Similarly, if the surface resists wetting, its resistance against wetting will increase when the surface becomes rough. The increase in wettability in the former or wetting resistance in the latter is attributed to the increase in surface area as the surface is roughened. The apparent contact angle on a fully wetted rough surface is given by the Wenzel equation Eq. (4.1)

$$\cos \boldsymbol{\theta}_{\mathrm{w}} = \boldsymbol{r} \cdot \cos \boldsymbol{\theta} \tag{4.1}$$

where $\boldsymbol{\theta}_{\mathrm{w}}$ is the Wenzel angle, $\boldsymbol{\theta}$ is the contact angle of the smooth surface of the same material, and $\boldsymbol{r}$ is the roughness factor. $\boldsymbol{r}$ is given by:

$$\boldsymbol{r} = \text{actual surface area / projected surface area} \tag{4.2}$$

In 1944, Cassie and Baxter [2] extended the analysis of the apparent contact angles for the wetting of porous surfaces similar to those encountered in textiles in clothing and feathers in birds. When a liquid wets a porous surface, air pockets are formed and the liquid–surface interface becomes a composite interface. Again, based on a simple thermodynamic argument, the apparent contact angle is determined by the energetics of the contact area under the liquid droplet, which has two components: one governs by the area fraction of the solid and the other by the area fraction of air. The general expression for the apparent contact angle ($\boldsymbol{\theta}_{\mathrm{app}}$) is:

$$\cos\boldsymbol{\theta}_{\mathrm{app}} = \boldsymbol{f}_1 \cdot \cos\boldsymbol{\theta}_1 + \boldsymbol{f}_2 \cdot \cos\boldsymbol{\theta}_2 \tag{4.3}$$

where $\boldsymbol{f}_1$ and $\boldsymbol{f}_2$ are the area fractions and $\boldsymbol{\theta}_1$ and $\boldsymbol{\theta}_2$ are the contact angles for the two components at the liquid–solid–air composite interface, respectively.

Since one of the components ($\boldsymbol{f}_2$) is air, $\cos 180° = -1$, Eq. (4.3) becomes the famous Cassie–Baxter equation:

$$\cos \theta_{\mathbf{CB}} = \boldsymbol{f} \cdot \cos \theta + (\boldsymbol{f} - 1) \tag{4.4}$$

where $\boldsymbol{\theta}_{\mathrm{CB}}$ is the Cassie–Baxter angle, $\boldsymbol{f}$ is the solid-area fraction, and $\boldsymbol{\theta}$ is the contact angle of the smooth surface of the same material.

As elucidated in Chap. 3, the angle of contact formed between a solid surface and the wetting liquid is a result of the mechanical equilibrium of the three surface tensions (γ_{SV}, γ_{LV} and γ_{SL}) acting on the three phase contact line. The contact angle is determined by the energetics at the contact line, not the contact area. So it comes as no surprise that there were once serious debates about the "right-or-wrong" of the Wenzel and Cassie–Baxter analyses [3–8]. Gao and McCarthy [3] reported a very simple experimental design to test the validity of Eq. (4.4). The test samples were prepared by first creating a textured spot of diameter d on a clean silicon wafer, followed by a fluorosilane treatment. The finished samples end up with a superhydrophobic spot within the hydrophobic silicon surface. Three spot diameters, 1, 1.5, and 2 mm, were fabricated. A schematic of the heterogeneous sample structure is given in Fig. 4.1.

Experimentally, a small droplet of water was dispensed to the center of the textured area. The diameter of the contact area D was recorded and the advancing/receding contact angles $\boldsymbol{\theta}_A/\boldsymbol{\theta}_R$ were determined. Small amount of water was added next. The diameter of the expanded drop and $\boldsymbol{\theta}_A/\boldsymbol{\theta}_R$ of the drop were determined. This procedure is repeated for other samples, and the data are summarized in Table 4.1.

Also included in Table 4.1 are the area fractions $\boldsymbol{f}_1$ and $\boldsymbol{f}_2$ calculated based on the dimensions of the spot and the contact area as well as the calculated $\boldsymbol{\theta}_A/\boldsymbol{\theta}_R$ values from Eq. (4.3). It is important to note that the calculated $\boldsymbol{\theta}_A/\boldsymbol{\theta}_R$ value varies as the solid-area fractions for the two surface components vary. For instance, the calculated $\boldsymbol{\theta}_A/\boldsymbol{\theta}_R$ would decrease as $\boldsymbol{f}_1$ (area fraction of the textured area) decreases. When $d > D$ such as the cases of Exp't # 1, 5, and 9, the $\boldsymbol{\theta}_A/\boldsymbol{\theta}_R$ values indicate that the textured area is superhydrophobic. On the other hand, when $d < D$, there is disagreement between the observed and the calculated values. Since the calculated value is entirely based on surface free energy consideration, it decreases gradually as $\boldsymbol{f}_1$ decreases. Experimentally, all cases with $d < D$ give identical $\boldsymbol{\theta}_A/\boldsymbol{\theta}_R$ values, indicating that the contact areas for Exp't # 2–4, 6–8, and 10–12 are all hydrophobic. The identical $\boldsymbol{\theta}_A/\boldsymbol{\theta}_R$ values coupled with the lack of correlation with the surface energetics of the contact area led Gao and McCarthy to conclude that it is the energetics at the contact line, not the contact area beneath the drop determines the contact angle [3]. While one may argue that the Cassie–Baxter equation is still useful in

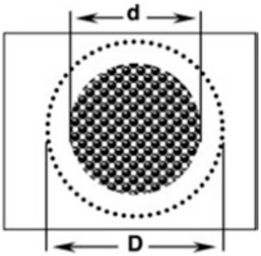

Fig. 4.1 Schematic of the heterogeneous surfaces fabricated on Si-wafer to test the Cassie–Baxter equation (*d* diameter of the texture, *D* diameter of the contact area during water contact angle measurement) (Reproduced with permission from [3], Copyright 2007 American Chemical Society)

Table 4.1 Physical and water contact angle data for the heterogeneous surfaces shown in Fig. 4.1 (data from [3])

Exp't #	d (mm)	D (mm)	f_1[a]	f_2[b]	θ_A/θ_R (cal'd)[c]	θ_A/θ_R
1	1	0.5	1.00	0.00		168°/132°
2	1	1.1	0.83	0.17	152°/122°	117°/81°
3	1	1.2	0.69	0.31	145°/115°	117°/82°
4	1	1.3	0.59	0.41	140°/108°	117°/81°
5	1.5	0.7	1.00	0.00		166°/134°
6	1.5	1.6	0.88	0.12	156°/125°	117°/82°
7	1.5	1.7	0.78	0.22	150°/119°	117°/81°
8	1.5	1.8	0.69	0.31	145°/115°	117°/82°
9	2	0.7	1.00	0.00		165°/133°
10	2	2.1	0.91	0.09	158°/126°	117°/82°
11	2	2.2	0.83	0.17	153°/122°	117°/81°
12	2	2.3	0.76	0.24	148°/118°	118°/82°

[a] f_1 area fraction of the textured area within the contact area
[b] f_2 area fraction of the non-textured area within the contact area
[c] Calculated from Eq. (4.3)

predicting the contact angle when the energetics between the contact line and the contact angle is the same. This is actually a weak argument with many flaws. This argument violates several related basic concepts that are the foundations of surface science. These basic concepts are: (1) the angle of contact between a solid and the wetting liquid is a result of a mechanical equilibrium for the three forces acting at the three phase contact line, not thermodynamic equilibrium, (2) contact angle is a one-dimensional, not two-dimensional phenomenon, and (3) surface tension and surface energy cannot be used interchangeably, the former is a tensor and the latter is scalar quantity without directional property. These basic concepts are not new. They have been discussed in fragments on-and-off from 1945 to 2010, e.g., by Pease [9], Bartell and Shepard [10], Johnson [11], Gray [12], Extrand [13], Gao and McCarthy [3, 8], and Bormashenko [14]. Although Gao and McCarthy did make an attempt to put their thoughts together and share it in their 2009 "Wetting 101°" paper [15], that effort appeared in vain as little has changed in the scientific community. We feel that this subject matter is so crucial to the future development of surface science that a second attempt is warranted. It is our hope that this work will play a role in laying a solid foundation for the basic concepts in surface science for years to come.

Together with additional results discussed later in this chapter, we agree with Gao and McCarthy that the uses of the Wenzel and Cassie–Baxter equations to predict contact angles and getting agreement are just fortuitous. In fact, many research groups [3, 16–19] have found disagreements between the calculated Wenzel and Cassie–Baxter angles with the experimentally measured contact angles, some of which will be further discussed below. We have to emphasize that we are by no means undermining the work of Wenzel and Cassie–Baxter. After all, these investigators did advance the knowledge of wetting rough surfaces and porous surfaces in the 30s and 40s, and their work had great influence to the field

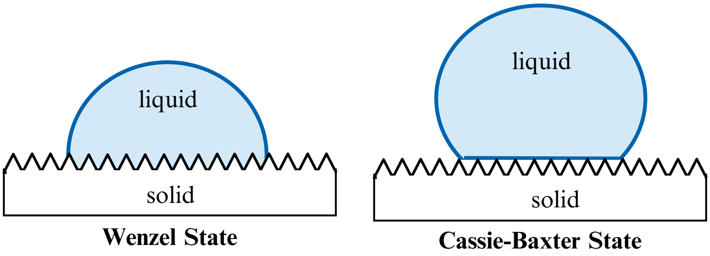

Fig. 4.2 Schematic of the two possible wetting states on rough surfaces

of surface science many decades after that. We should consider that recognizing and accepting the shortfall of the Wenzel and Cassie–Baxter analyses by itself is an important progress in surface science. Fundamentally, when a liquid wets a rough surface, there are two possible wetting states, one with the liquid fully wetting every area of the rough surface and the other with the liquid partially wetting and pinning on the asperities of the rough surface. The latter results in the formation of air pockets and a liquid–solid–air composite interface. These two wetting states have appropriately been recognized as the Wenzel and Cassie–Baxter state, respectively, in the literature (Fig. 4.2).

4.2 Wetting in the Wenzel State

According to the Wenzel equation Eq. (4.1), rough surface made of hydrophilic material can render itself superhydrophilic with a very small water contact angle $\boldsymbol{\theta}$ of <10°. Rough surfaces with moderately hydrophilic and hydrophobic materials, on the other hand, can result in surfaces with large contact angles. Conceptually, when a surface is fully wetted by a liquid, it implies that the wetting process is energetically favorable. Crucial questions remain and they are: will the liquid droplet be in the most stable wetting state? What determines the contact angle? How does the contact line look like? What are the factors that control the movement of liquid on the rough surfaces? These questions will be addressed in the following.

4.2.1 The Metastable and Most Stable Wetting State

In 2004, Meiron, Marmur, and Saguy [16] reported the fabrication of four rough surfaces by coating beeswax on a glass slide and three abrasive papers (attached to glass slides) of roughness ranging from Wenzel roughness factor $\boldsymbol{r}$ 1.03–1.25 as determined by the grit number of the abrasive paper. The surface energy of these surfaces should be very similar as they were prepared from the same beeswax. The contact angles of water and ethylene glycol on these four surfaces were studied before and after vibration with a loudspeaker. The product $\boldsymbol{fA}$ represents the velocity

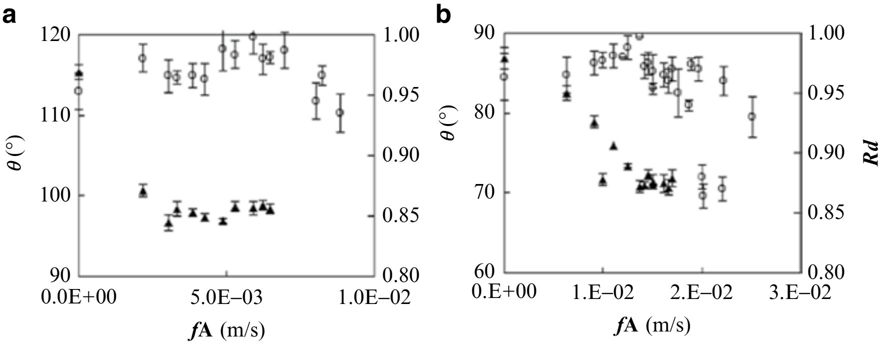

Fig. 4.3 Plot of contact angle (***θ***) and drop roundness (***Rd***) as a function of vibration velocity ***fA*** for surface with ***r*** = 1.09 (**a**) water and (**b**) ethylene glycol (*open circle* before and *filled triangle* after vibration) (Reproduced with permission from [16], Copyright 2004 Elsevier)

of the vibration motion generated by the loudspeaker. Plots of the effect of ***fA*** on the contact angle and roundness (***Rd***) of the droplets for water and ethylene glycol are shown in Fig. 4.3 for surface with ***r*** = 1.09. Typically, drops with ***Rd*** > 0.95 are considered round.

The results clearly show that vibration of the droplets using the loudspeaker de-pins the contact lines and brings the drops to the more stable wetting states with smaller contact angles. The Wenzel contact angles ($\boldsymbol{\theta}_{\mathrm{W}}$) for water and ethylene glycol initially at ~115° and ~85°, respectively, were shown to decrease and subsequently level off at ~98° and ~71°, respectively, after vibration. The results suggest that the initial sessile droplets for both water and ethylene glycol are metastable. Appropriate vibration brings the metastable wetting states to their respective most stable wetting states with equilibrium angles at $\boldsymbol{\theta}_{\mathrm{W}}^{\mathrm{eq}}$. A schematic showing the free energy relationship between the initial contact angle $\boldsymbol{\theta}_{\mathrm{W}}$ and the equilibrium contact angle $\boldsymbol{\theta}_{\mathrm{W}}^{\mathrm{eq}}$ is given in Fig. 4.4.

This free energy relationship is actually supported by the data in Fig. 4.3. For instance, the viscosity for ethylene glycol is higher than that of water, suggesting that the energy barrier for the liquid advance is higher for ethylene glycol on the same rough surface. Indeed, comparison of the ***fA*** values in Fig. 4.3a, b reveals that it takes about ten times more energy to bring the ethylene glycol droplet to the equilibrium state as compared to that of water. Table 4.2 compares the observed $\boldsymbol{\theta}_{\mathrm{W}}^{\mathrm{eq}}$ values for water and ethylene glycol on the four rough surfaces with the calculated Wenzel angle $(\boldsymbol{\theta}_{\mathrm{W}})^{\mathrm{cal}}$ values from the Wenzel equation Eq. (4.1). A very good agreement is obtained. The agreement confirms that, as with smooth surface, the apparent contact angle $\boldsymbol{\theta}_{\mathrm{W}}$ on rough surface is from a metastable wetting state. Liquid droplet just ceases to spread as all of its kinetic energy is dissipated due to friction created by the rough surface. This results in a larger than expected $\boldsymbol{\theta}_{\mathrm{W}}$ value. When the metastable wetting state is excited by the vibration noise, the contact line de-pins and continues to advance to the most stable wetting state with an equilibrium angle $\boldsymbol{\theta}_{\mathrm{W}}^{\mathrm{eq}}$.

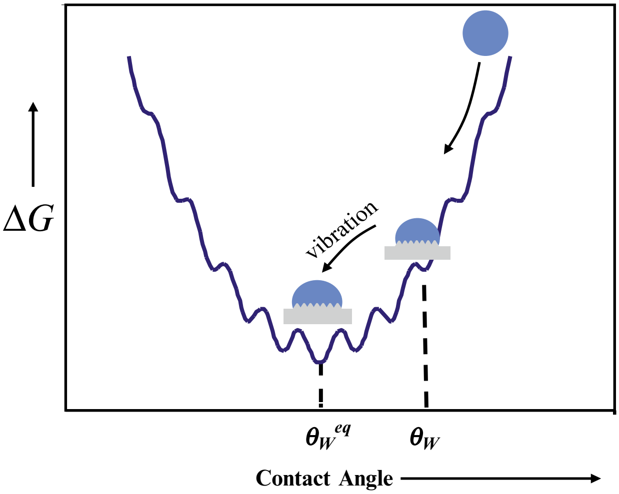

Fig. 4.4 Schematic of the free energy relationship between Wenzel angle $\boldsymbol{\theta}_{\mathrm{W}}$ and the equilibrium contact angle $\boldsymbol{\theta}_{\mathrm{W}}^{\mathrm{eq}}$ on rough surface

Table 4.2 Comparison of equilibrium Wenzel angle $\boldsymbol{\theta}_{\mathrm{W}}^{\mathrm{eq}}$ with the calculated Wenzel angle $(\boldsymbol{\theta}_{\mathrm{W}})^{\mathrm{cal}}$ (data taken from [16])

	Water		Ethylene glycol	
r	$\boldsymbol{\theta}_{\mathrm{W}}^{\mathrm{eq}}$	$(\boldsymbol{\theta}_{\mathrm{W}})^{\mathrm{cal}}$	$\boldsymbol{\theta}_{\mathrm{W}}^{\mathrm{eq}}$	$(\boldsymbol{\theta}_{\mathrm{W}})^{\mathrm{cal}}$
1.01	97.3	97.3	73.1	73.2
1.03	97.9	97.7	72.4	72.9
1.09	98.0	97.3	71.6	73.2
1.25	100.1	98.1	69.7	73.9

4.2.2 Unexpected Wettability

The Wenzel equation suggests that roughness should increase the wettability of hydrophilic surface. This is certainly true for highly hydrophilic materials (water $\boldsymbol{\theta} < 30°$), where roughness has often led to super-wetting or superhydrophilicity [20]. On the other hand, the wetting behavior of rough surface made of moderately hydrophilic material has not been well studied. In 2010, Forsberg and co-workers [17] reported a study of the wetting of microtextured surfaces comprising square pillar arrays made of SU8. SU8 is a common photoresist material used in photolithography. It is moderately hydrophilic with a water $\boldsymbol{\theta}$ of ~72°. Figure 4.5a, b show the schematics of the pillar array design. The width of the square pillar is fixed at $w = 20$ μm, the pitch d varies from 25 to 120 μm, and the heights studied are at 7 and 30 μm. Figure 4.5c shows the water advancing and receding angle of the control smooth SU8 surface, which is at 72° and 59°, respectively. On the pillar array surface shown in Fig. 4.5d ($w/d = 0.63$, height 7 μm), an unexpected large advancing contact angle at 140° was observed. The surface exhibits practically 0° receding angle and a photograph showing the meniscus after water receding is shown in the insert. The result suggests that water fully wets the SU8 pillar array surface. Additional control experiment was performed with a hydrophobized pillar array

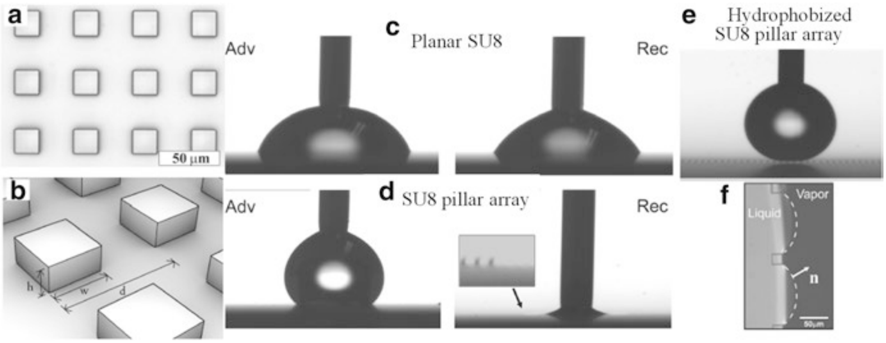

Fig. 4.5 (**a**, **b**) Schematics for the square pillar array model surfaces, (**c**) advancing and receding contact angle data for the smooth SU8 surface, (**d**) advancing and receding contact angle data for an SU8 pillar array surface ($w/d = 0.63$, $h = 7$ µm), (**e**) water sessile drop data on a hydrophobized SU8 pillar array surface, and (**f**) photograph of the advance contact line ($d = 120$ µm) (Reproduced with permission from [17], Copyright 2010 American Chemical Society)

Fig. 4.6 Plot of cos*θ* versus *w/d* for SU8 square pillar array surfaces (Reproduced with permission from [17], Copyright 2010 American Chemical Society)

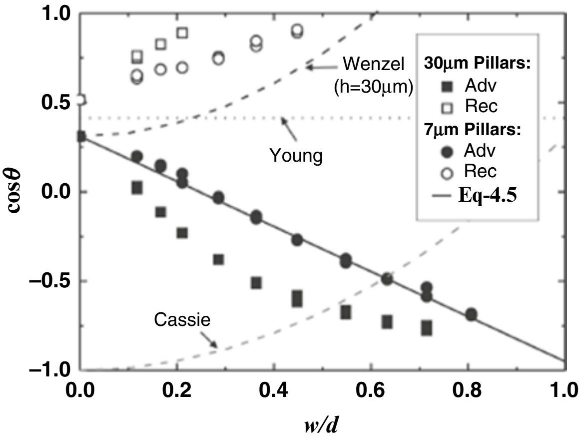

surface. The sessile drop data is given in Fig. 4.5e. A large static contact angle with small hysteresis was obtained, indicating that the water droplet is indeed in the Cassie–Baxter state on the hydrophobized pillar array surface. The overall wetting data allow one to conclude that water droplet is in the Wenzel state on the SU8 pillar array surfaces.

Figure 4.6 plots the advancing and receding contact angles of the SU8 pillar array surfaces as a function of *w/d*. The upper dash line shows the trend calculated from the Wenzel equation Eq. (4.1). The observed advancing contact angles and the calculated data are not only in disagreement, they are actually trending in an opposite direction. A closer examination of the advancing contact line on the pillar array surface (Fig. 4.5f) shows that the contact line pins at the corners of the square and extends outward in the space between pillars. To explain the unexpected large contact angle and the disagreement between the Wenzel equation and the experimental data, Forsbery and co-workers [17] first assumed that the liquid–solid–air interface is in a mechanically stable configuration. They then used the dimension and geometry of the contact line to modify the Wenzel roughness factor. The modified Wenzel equation is given by:

$$\cos\theta_{\mathrm{W}}^{\mathrm{mod}} = \left(1 - \frac{w}{d}\right) \cdot \cos\theta_{\mathbf{SU8}} + \left(\frac{w}{d}\right) \cdot \cos\left(\theta_{\mathbf{SU8}} + \frac{\pi}{2}\right) \tag{4.5}$$

The $\cos\theta_{\mathrm{W}}^{\mathrm{mod}}$ values were calculated and shown as the solid line in Fig. 4.6. A very good agreement is obtained between the modified Wenzel angle and the observed angle for the pillar array surfaces with a 7 μm pillar height. For pillar array surfaces of 30 μm pillar height, the observed apparent contact angles were even larger. The discrepancy with the calculated values from Eq. (4.5) is attributable to the assumption of using a low pillar height in the modified equation. In any event, this study again supports the notion that contact angle is governed by where the contact line is pinned, not the contact area beneath the liquid droplet.

The experimental observation by Forsbery and co-workers is consistent with the wetting dynamics on solid surfaces as discussed in Chap. 3. For instance, as water starts wetting the 7 μm pillar array surface, the contact line advances. The advance will cease when all its kinetic energy is dissipated. Due to the large friction created by the pillar array, the advance contact line is stopped far from its equilibrium position, resulting in an unexpected large contact angle, consistent with the free energy model shown in Fig. 4.4. This interpretation gains further support from the data collecting from the 30 μm pillar height, pillar array surfaces. Due to the increase in pillar height, the energy barrier or friction against wetting is larger for the 30 μm pillar array surfaces. The analysis would suggest that the advancing contact angles for the 30 μm pillar height surfaces would be larger than those of the 7 μm pillar height surfaces. Indeed, this is experimentally observed.

4.2.3 Roughness Geometry on Wettability and Wetting Dynamics

A series of model rough PDMS surfaces comprising arrays of 3 μm hemispherical bumps and cavities with pitches ranging from 4.5 to 96 μm were recently fabricated by Kanungo and co-workers using the conventional photolithography and molding techniques [19]. The representative SEM micrographs are given in Fig. 4.7. These surfaces are designed to address the following questions: are surfaces with bumps and cavities better models to emulate wetting and de-wetting behavior of liquid on real, practical rough surfaces, which are mostly hills and valleys? The wetting entrant angles between real rough surfaces and the bumpy and cavity surfaces shown in Fig. 4.7 are fairly comparable, significantly less than 90°. Whereas majority of the model rough surfaces reported in the literature are pillar arrays with high

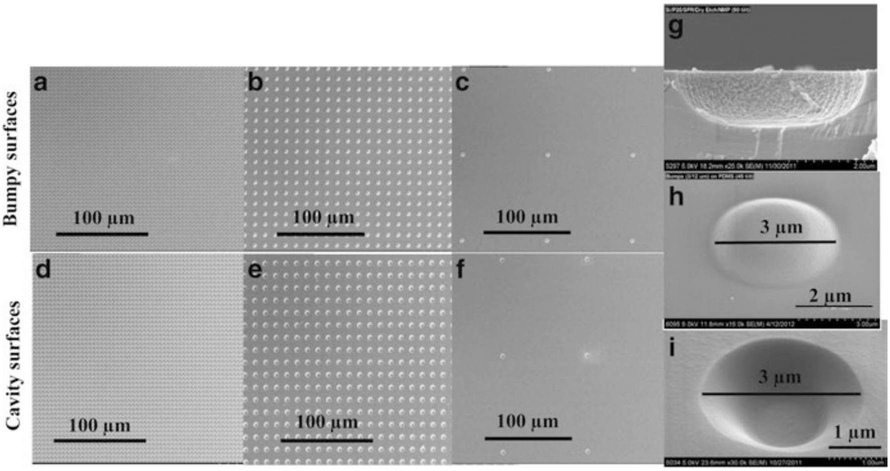

Fig. 4.7 Representative SEM micrographs of rough PDMS surfaces with varying pitches (**a**, **d** 4.5 µm, **b**, **e** 12 µm and **c**, **f** 96 µm); (**g**) SEM micrograph of the 3 μm diameter hemispherical silicon mold, (**h**) SEM micrograph of the hemispherical bump on the PDMS surface created from the mold in (**g**), and (**i**) SEM micrograph of the hemispherical cavity PDMS surface molded from the bumpy surface in (**g**) (Reproduced with permission from [19], Copyright 2014 American Chemical Society)

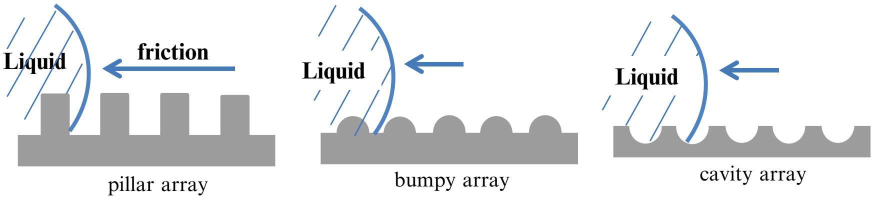

Fig. 4.8 Schematic of the wetting scenarios between a pillar array rough surface and the hemispherical bumpy and cavity array surfaces

aspect ratios [17, 21–23]. Pillars are vertical protrusions from a flat surface and the wetting entrant angle against the advancing liquid is at 90°. The friction the pillars exerted to the advancing liquid is expected to be larger than those from hills and valleys and also from bumps and cavity surfaces based on simple geometrical consideration. Schematics showing the differences in frictions created by these surfaces are shown in Fig. 4.8. Other objectives of the work include study of the effect of rough geometry, using bumps and cavities as models for hills and valleys, on surface wettability and wetting dynamics.

Wetting States on Model Rough PDMS Surfaces. The surface properties of all model bumpy and cavity PDMS surfaces were studied by static and dynamic contact angle measurements with water as the test liquid and the data are tabulated in Table 4.3. The contact angle data for the smooth PDMS surface are included as reference. As discussed in Sect. 4.1, wetting of liquid on a rough surface can be described by

Table 4.3 Contact angle measurement data for model rough PDMS surfaces with arrays of bumps and cavities (Reproduced with permission from [19], Copyright 2014 American Chemical Society)

				Array of bumps				Array of cavities				[i] $\boldsymbol{r}^{\mathrm{eff}}$	[j] $\boldsymbol{\theta}_{\mathrm{W}}^{\mathrm{mod}}$
Pitch[a]	$\boldsymbol{r}$[b]	$\boldsymbol{\theta}_{\mathrm{W}}$[c]	$\boldsymbol{\theta}_{\mathrm{CB}}$[d]	$\boldsymbol{\theta}$[e]	$\boldsymbol{\theta}_{\mathrm{A}}$[f]	$\boldsymbol{\theta}_{\mathrm{R}}$[g]	**CAH**[h]	$\boldsymbol{\theta}$[e]	$\boldsymbol{\theta}_{\mathrm{A}}$[f]	$\boldsymbol{\theta}_{\mathrm{R}}$[g]	**CAH**[h]		
96 µm	1.00	110°	110°	116°	117°	69°	48°	117°	120°	76°	44°	1.05	111°
48 µm	1.01	110°	110°	115°	119°	71°	48°	117°	120°	77°	43°	1.11	112°
24 µm	1.02	111°	110°	117°	120°	68°	52°	118°	119°	79°	40°	1.22	115°
12 µm	1.1	112°	112°	122°	125°	61°	64°	124°	129°	81°	48°	1.44	119°
6 µm	1.4	118°	118°	129°	131°	68°	63°	128°	132°	83°	49°	1.87	130°
4.5 µm	1.7	126°	125°	138	144°	83°	61°	136°	140°	88°	52°	2.16	138°
Smooth surface	1.00	–	–	110°	112°	72°	40°	–	–	–		–	–

[a] Center-to-center spacing between bumps or cavities

[b] The classic Wenzel roughness ratio, actual surface area divided by projected area

[c] Calculated Wenzel angle from Eq. (4.1)

[d] Calculated Cassie–Baxter angle ($\boldsymbol{\theta}_{\mathrm{CB}}$) for cavity surface from Eq. (4.2)

[e] Static contact angle

[f] Advancing contact angle

[g] Receding contact angle

[h] Contact angle hysteresis, defined as ($\boldsymbol{\theta}_{\mathrm{A}}$–$\boldsymbol{\theta}_{\mathrm{R}}$)

[i] Effective roughness factor calculated by correcting for the increase of contact line density at the three-phase contact line [17]

[j] Modified Wenzel angle calculated according to method of Forsberg and co-workers [17]

the two classic wetting models. When the rough surface is fully wetted by the liquid, the apparent static contact angle is the Wenzel angle ($\boldsymbol{\theta}_{\mathrm{W}}$) and is given by the Wenzel equation [1]. The Wenzel roughness ratios ($\boldsymbol{r}$) for the model rough PDMS surfaces can be calculated from the radii and geometry of the bumps and cavities. The $\boldsymbol{r}$ values are the same for the bumpy and cavity surfaces of the same pitch. Details of the calculation have been given elsewhere [19]. From the $\boldsymbol{r}$ values, the Wenzel angles ($\boldsymbol{\theta}_{\mathrm{W}}$) are calculated and are given in Table 4.3 column 3.

For rough, porous surface where pockets of air can be created during wetting, a composite liquid–solid–air interface is formed. The apparent contact angle is the Cassie–Baxter angle ($\boldsymbol{\theta}_{\mathrm{CB}}$) and is given by the Cassie–Baxter equation [2]. Figure 4.9 shows the generalized, hypothetical wetting states for (a) the bumpy PDMS surface and (b) the cavity PDMS surface. On the bumpy PDMS surface, h_{L} is the height needed to create the air pocket. On the cavity surface, h_{L} is the sagging height. Since optical microscopy results (Fig. 4.10 below) indicate that the contact lines for both bumpy and cavity surfaces are pinned at the lead edge of the rough structures, that means $h_{\mathrm{L}}=0$ for both the bumpy and cavity surfaces. It is thus geometrical impossible to trap air on the bumpy surface when $h_{\mathrm{L}}=0$ during wetting. In the other word, bumpy PDMS surfaces will always be in the Wenzel wetting state. However, a Cassie–Baxter state is still a possibility for the cavity surface when $h_{\mathrm{L}}=0$. The Cassie–Baxter angles ($\boldsymbol{\theta}_{\mathrm{CB}}$) for cavity surfaces are then calculated (Table 4.3 column 4).

The overall results in Table 4.3 show that the observed $\boldsymbol{\theta}$ for the model rough PDMS surfaces (columns 5 and 9) are not in agreement with neither $\boldsymbol{\theta}_{\mathrm{W}}$ nor $\boldsymbol{\theta}_{\mathrm{CB}}$

Fig. 4.9 Generalized, hypothetical schematics for the wetting of (**a**) the bumpy PDMS surface and (**b**) the cavity PDMS surface. On the bumpy PDMS surface, h_L is the height needed to create the air pocket. On the cavity surface, h_L is the sagging height (Reproduced with permission from [19], Copyright 2014 American Chemical Society)

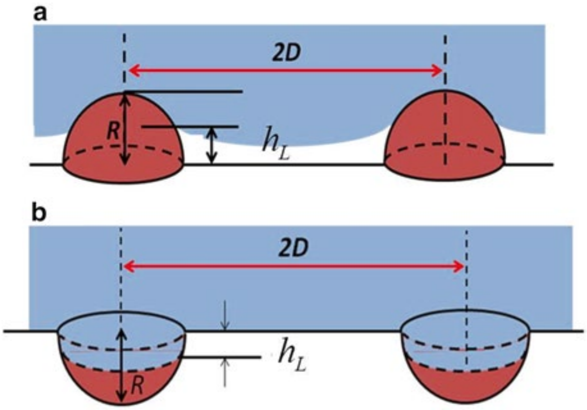

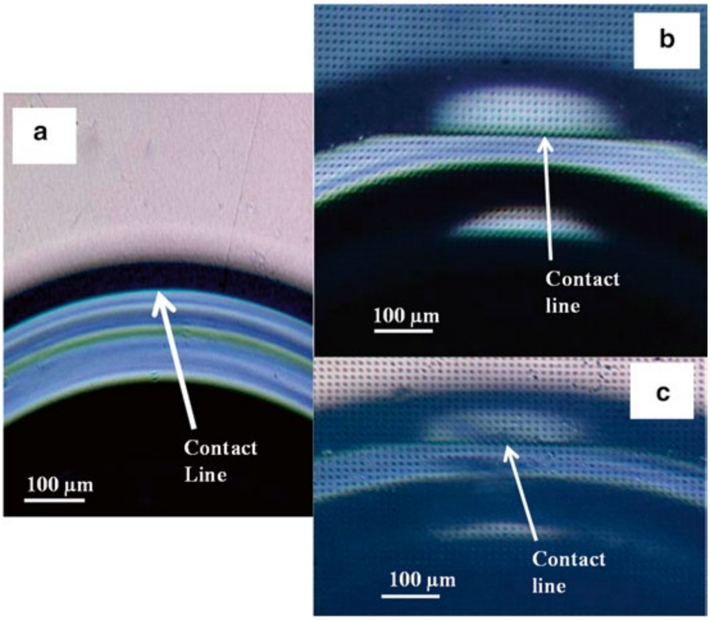

Fig. 4.10 Optical photographs of the three-phase contact lines as imaged from the bottom of the water sessile droplets on (**a**) smooth, (**b**) 12 μm pitch bumpy, and (**c**) 12 μm pitch cavity PDMS surfaces (Reproduced with permission from [19], Copyright 2014 American Chemical Society)

values. The disagreement is not surprising as recent theoretical and experimental results showed that the contact angles of rough surfaces tend to correlate more to the locality of the three phase contact line than the classic Wenzel and Cassie–Baxter angles due to pinning of the contact lines on rough surfaces [17, 18, 24–27]. Using the methodology of Forsberg and co-workers [17], a one-dimensional modified

Wenzel equation can be derived based on the geometry of the contact line (Fig. 4.10), where $\boldsymbol{\theta}_{\mathrm{W}}^{\mathrm{mod}}$ is the modified Wenzel angle.

$$\cos \theta_{\mathrm{W}}^{\mathrm{mod}} = \left(1 - \frac{R}{D}\right) \cdot \cos \theta + \left(\frac{R}{D}\right) \cdot \cos\left(\theta + \frac{\pi}{2}\right) \tag{4.6}$$

After rearranging the above equation to the classical Wenzel format, the effective roughness ratio (r^{eff}) is obtained and is given by:

$$\boldsymbol{r}^{\mathrm{eff}} = 1 - \frac{R}{D}\left(1 + \tan \theta\right) \tag{4.7}$$

Details for the derivations of $\boldsymbol{r}^{\mathrm{eff}}$ and $\boldsymbol{\theta}_{\mathrm{W}}^{\mathrm{mod}}$ and discussion of the wetting states have been given earlier [19]. The calculated $\boldsymbol{r}^{\mathrm{eff}}$ and $\boldsymbol{\theta}_{\mathrm{W}}^{\mathrm{mod}}$ values are listed in Table 4.3 columns 13 and 14, respectively. Without exception, reasonably good agreements between $\boldsymbol{\theta}_{\mathrm{W}}^{\mathrm{mod}}$ and $\boldsymbol{\theta}$ are observed for both bumpy and cavity surfaces, suggesting that both type of surfaces are in the fully wetted Wenzel states. This conclusion is supported by recent wetting studies of PDMS pillar array surfaces both theoretically and experimentally. Jopp et al. [28] showed by free energy calculation that water will fill all the grooves between pillar arrays of PDMS, which is hydrophobic. Papadopoulos and co-workers [22] reported visualization of the fully wetted liquid–solid interface between water and PDMS three dimensionally by laser scanning confocal microscopy. Additional evidence supporting the conclusion that water is in the fully wetted Wenzel state on both bumpy and cavity PDMS surfaces come from the drop vibration experiments, which will be given later in this chapter.

Advancing and Receding Contact Lines The location and the geometry of the advancing contact lines on the bumpy and cavity PDMS surfaces were examined directly from the bottom of the water droplets and the optical micrographs of the contact lines are given in Fig. 4.10. Expectedly, the contact line for the smooth PDMS surface is smooth and round (Fig. 4.10a), whereas those on the bumpy and cavity surfaces are distorted by the microstructures (Fig. 4.10b, c). This is consistent with the contact lines observed in other microtextured surfaces, where the three-phase contact lines are all shown to follow the edge of the rough microstructures [18, 21, 22, 24–27]. A closer examination of the photographs reveals that the three-phase contact lines in Fig. 4.10 actually follow the lead edges of the bumps on the bumpy surface and the cavities on the cavity surface. A schematic showing the top-view and side-view of the three-phase contact lines on these surfaces is given in Fig. 4.11. Both contact lines are shown pinning at the lead edges of the rough structures.

Surfactants and dyes in aqueous solutions are known to localize around the three-phase contact lines [29]. As water is evaporated, the dye crystalizes and the residues provide a trace for the receding contact line. Using the procedure analogous to that reported by Wu and co-workers [30], the receding contact lines were imaged by evaporating the sessile droplets of a very dilute Rhodamine solution (~5×10^{-6} g/mL) on the smooth and the bumpy and cavity PDMS surfaces. Controlled experiments show that the added dye in water has no effect on the contact angles on all PDMS surfaces. Figure 4.12a–c show the optical photographs of the evapo-

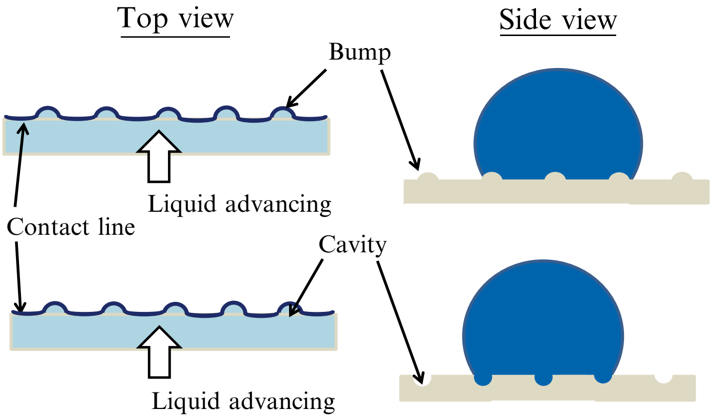

Fig. 4.11 Schematics for the top-view and side-view of the three-phase contact lines for water droplets on the bumpy and cavity PDMS surfaces (Reproduced with permission from [19], Copyright 2014 American Chemical Society)

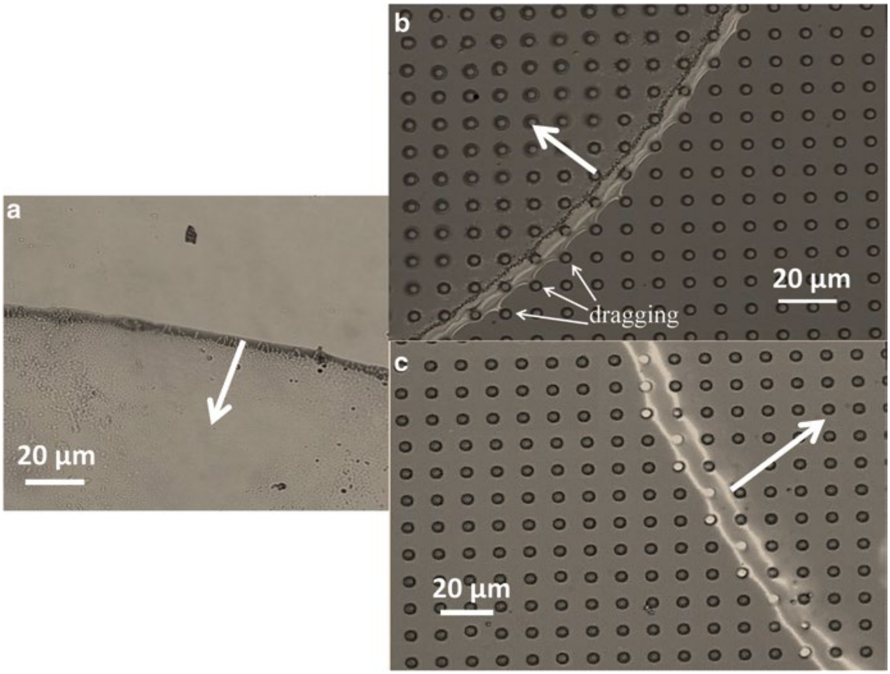

Fig. 4.12 Optical photographs of the receding contact lines as imaged by evaporating a very dilute Rhodamine dye solution (~5×10^{-6} g/mL) on (**a**) smooth, (**b**) 12 µm pitch bumpy, and (**c**) 12 µm pitch cavity PDMS surfaces. The arrows show the receding directions (Reproduced with permission from [19], Copyright 2014 American Chemical Society)

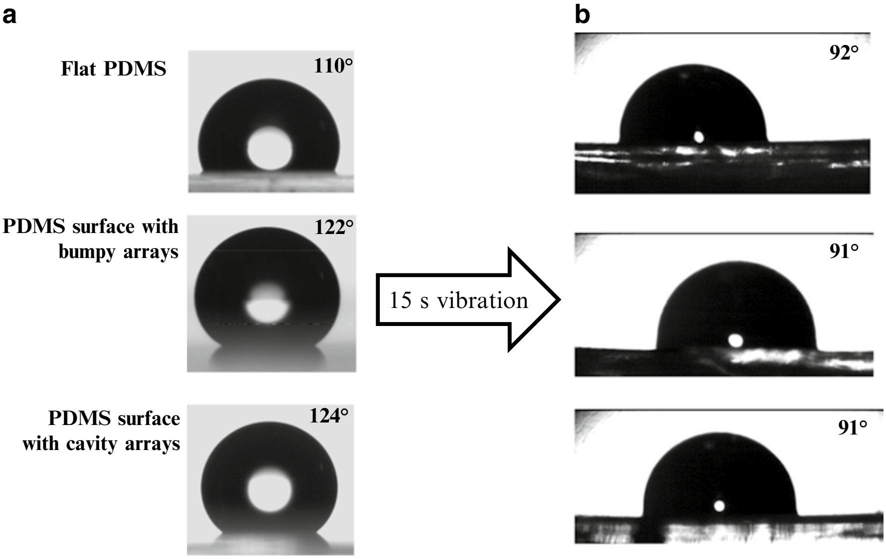

Fig. 4.13 Images of the water sessile droplets on smooth and rough PDMS surfaces (**a**) before and (**b**) after 15 s vibration (Reproduced with permission from [19], Copyright 2014 American Chemical Society)

rated droplets on the smooth PDMS surface and the bumpy and cavity PDMS surfaces, respectively. The photograph in Fig. 4.12a clearly shows the dye residue on the smooth PDMS surface after water evaporation. The contact line is round and smooth during the liquid-receding process. On the other hand, microstructures are visible in the receding contact line on the bumpy PDMS surface (Fig. 4.12b). The image suggests that the bumps are dragging the contact line as the liquid is receding. As for the cavity surface, the receding contact line is relatively smooth and round. There appears to be little dragging by the cavities. The microscopy results thus indicate that rough geometry does have an effect on the movement of the contact line. Bumps are found to drag the contact line as it recedes while cavities behave like a smooth surface.

Drop Vibration Experiments Fig. 4.13a depicts the photographs of the ~5 μL sessile water droplets on the smooth PDMS surface, the 12 μm pitch bumpy PDMS surface, and the 12 μm pitch cavity PDMS surface. Their static contact angles are at 110°, 122°, and 124°, respectively. To test the wetting states of the water on these surfaces, Kanungo and co-workers [19] subjected all three water droplets in Fig. 4.13a a 15-s vibration according to the procedure described by Cwikel and co-workers [31] and the results are given in Fig. 4.13b. All three sessile droplets give the same static contact angles at ~91° after the 15-s vibration. The results indicate that all three sessile droplets were in the metastable wetting states before the vibration. While the static contact angle for the smooth PDMS surface changes from 110° to 92° after vibration and the observation is consistent with that reported

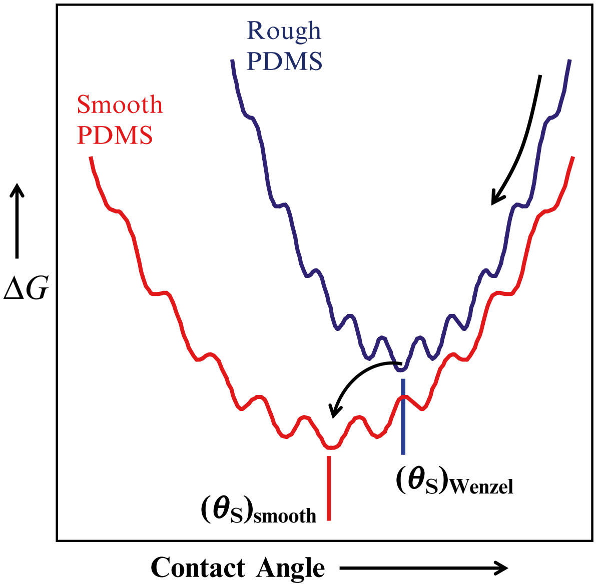

Fig. 4.14 Schematic plot of the Gibbs free energy curves for wetting of a smooth PDMS surface and rough PDMS surface (bumps and cavities) by water as a function of the apparent contact angle. $\boldsymbol{\theta}_S$ is the most stable contact angle (Reproduced with permission from [19], Copyright 2014 American Chemical Society)

by Cwikel and co-workers [31], the results for the bumpy and cavity surfaces are very unusual as their contact angles after vibration would suggest that the water droplets pin selectively in the smooth areas of the rough PDMS surface! Indeed, further optical microscopy study reveals that, the contact lines on both bumpy and cavity PDMS surfaces become much smoother after vibration and that they appear to be on the smooth area of the PDMS surfaces rather than distorted by the rough structures [19]. The overall results from the drop vibration experiments suggest that water droplets are always in the metastable wetting states on the bumpy and cavity surfaces due to pinning effect. Vibration, which leads to de-pinning and relocation of the contact lines, results in the population of the most stable wetting states on these surfaces. The similar final $\boldsymbol{\theta}$ values for all the PDMS surfaces after vibration suggest that the most stable wetting states on the bumpy and cavity surfaces also involve pinning the water droplets in the smooth area of the rough PDMS surfaces. The observation can be rationalized based on the Gibbs free energy curves of the wetting states of the smooth and rough surfaces. The schematics of the curves are given in Fig. 4.14 based on the contact angle data in Table 4.3. As discussed in Chap. 3 and Sect. 4.2, wetting a solid surface involves transfer of the kinetic energy in the sessile droplet (gained from gravity acceleration) to the kinetic energy for wetting after the liquid droplet contacts the surface. The droplet will cease to spread when all its kinetic energy is dissipated. The generally large $\boldsymbol{\theta}$ values observed in Table 4.3 for the bumpy and cavity PDMS surfaces relative to the calculated Wenzel angles ($\boldsymbol{\theta}_{\mathrm{W}}$) can thus be attributed to this pinning effect [17, 22, 26]. In the case of a fully wetted water droplet on a rough surface, Meiron and co-workers [16] showed that vibration can convert a metastable wetting state to the most stable Wenzel state. The contact angle for the stable Wenzel state was found to be in agreement with the calculated Wenzel angle ($\boldsymbol{\theta}_{\mathrm{W}}$). In the cases of the model PDMS surfaces in the Kanungo study, contrast to that reported by Meiron and co-workers, the most stable contact angles for the bumpy and cavity surfaces are a lot smaller than the calculated $\boldsymbol{\theta}_{\mathrm{W}}$ (110°–126° vs. ~91°). The similar contact angles for all three PDMS surfaces after the 15-s vibration suggest that the contact lines on the rough surfaces relocate to the smooth area of the PDMS surface after de-pinning by vibration. This is supported by recent optical microscopy results and implies that the stable Wenzel states for the bumpy and cavity surfaces are not as thermodynamically favorable as that of the smooth surface. We suggest that during vibrational excitation, the contact lines de-pin and the droplets on the bumpy and cavity surfaces are able to cross-over to the energy curve of the smooth PDMS surface (Fig. 4.14).

Effects of Pitch Length and Geometry on Wettability. Results in Table 4.3 show that the static contact angles ($\boldsymbol{\theta}$) increases as pitch length decreases for both types of rough surfaces (bumps and cavities) due to the increase in roughness on the PDMS surface. It is worthy pointing out that for the same pitch, where the roughness ratio is the same, the static contact angles for the bumpy and cavity surface are actually very similar.

Interesting results are observed for the dynamic contact angle data. The advancing contact angle ($\boldsymbol{\theta}_{\mathrm{A}}$) for the bumpy surface and the cavity surface are comparable for the same pitch and they increase, from ~116° to ~138°, as $\boldsymbol{r}^{\mathbf{eff}}$ increases from 1.05 to 2.16. Although similar trend is also observed for the receding contact angles ($\boldsymbol{\theta}_{\mathrm{R}}$) (increase as $\boldsymbol{r}^{\mathrm{eff}}$ increases), the receding angles for the bumpy surfaces are consistently smaller than those of the cavity surfaces. In the other word, for the same pitch, the hysteresis for the bumpy PDMS surface (column 8) is always larger than that of the cavity surface (column 12). Similar asymmetric hysteresis has been observed for pillar and porous array surfaces by Priest et al. [21]. In the case of the bumpy and cavity PDMS surfaces, Kanungo et al. actually have visual evidence to show that bumps are exerting strong resistance and drag the receding contact line (Fig. 4.12b) whereas minimal dragging is seen by the cavities (Fig. 4.12c). These authors thus attribute the asymmetric hysteresis observed to the dragging of the contact line by the bumps as the liquid recedes [19].

4.2.4 Practical Consequences

Being able to wet every cavity or hole in a rough surface has advantages in both nature and man-made devices. When water wets a superhydrophilic surface, it spreads spontaneously with no trap air and no measurable contact angle. In nature, such surface structures have been created in plant leaves so that the plants can adapt

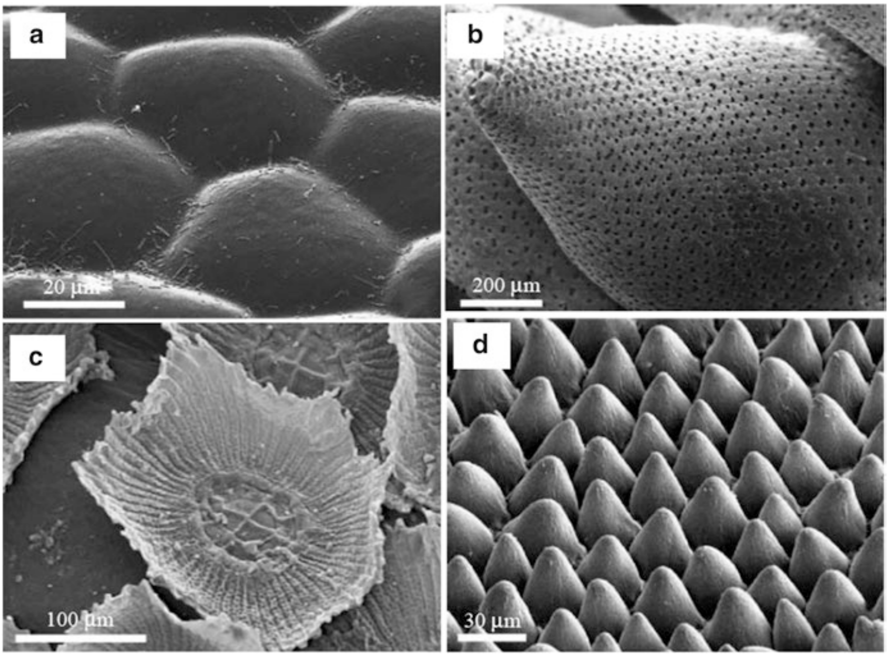

Fig. 4.15 SEM micrographs of some superhydrophilic plant leaves (**a**) Anubias barteri, (**b**) Sphagnum squarrosum, (**c**) Spanish moss *Tillandsia usneoides*, and (**d**) *Calathea zebrina* (Reproduced with permissions from [32], Copyright 2008 The Royal Society of Chemistry and [33] Copyright 2009 Elsevier)

and survive in their perspective living environment [32, 33]. For instance, the microstructures in submerging water plant leaves tend to be smooth, enabling water to evenly wet the surface while discourage fouling (Fig. 4.15a). Contrarily, the microstructures of water-absorbing plants, such various mosses, are structurally more complex (Fig. 4.15b, c). These leaves are for uptake of water and nutrient, so the surface is designed to be superhydrophilic with a structure to hold onto the absorbed water. On the other hand, plant leaves from *Calathea zebrina* (Fig. 4.15d) will have a very simple microstructure because all it needs to do is to spread water very fast on the surface.

Owing to the super-spreading ability, researchers have envisioned that superhydrophilic surfaces should enable antifogging as minute water droplets will spread instead of pinning and fogging the surface. Similarly, the spreading action leads to wet self-cleaning as dust and dirt particles will wash away during water spreading. Many artificial superhydrophilic surfaces are known and the most notable one is the film of TiO_2 [34]. The surface is prepared by coating a sol gel precursor on a substrate followed by annealing the coated film in a furnace. TiO_2 film is intrinsically, moderately hydrophilic. Its superhydrophilicity is activated by UV or sunlight radiation. Antifogging devices and self-cleaning structures (Fig. 4.16) have been commercialized, and the subject has been reviewed in the literature [35]. Similarly to

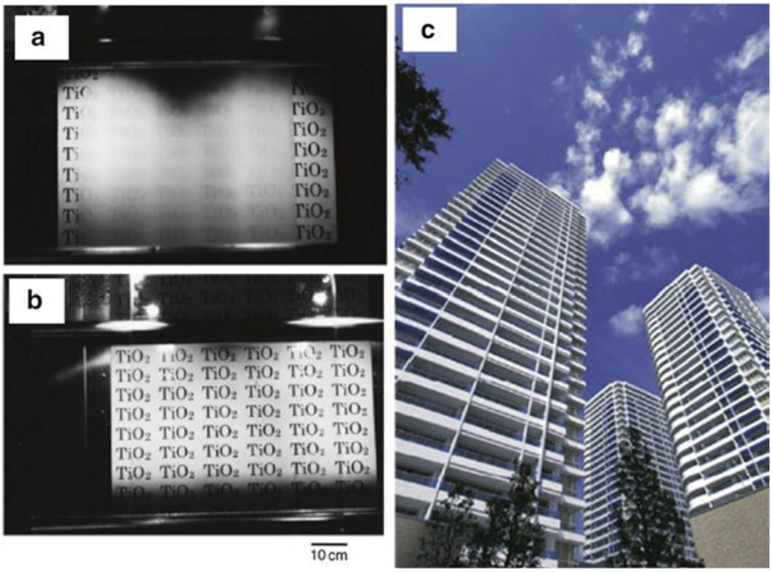

Fig. 4.16 (**a**) Photograph of a foggy TiO_2 coated glass, (**b**) surface in (**a**) after sufficient UV illumination, and (**c**) photograph of the MM Towers in Yokohama, Japan where self-cleaning tiles were used (Reproduced with permission from [35], Copyright 2008 Elsevier)

TiO_2, silica and other metal oxide particles are hydrophilic too. They can be incorporated into thin films via the sol gel technique [36], or by layer-by-layer deposition [37] or as a composite coating with a polymer binder [38]. Finally, a fully wetted liquid–solid interface should also be beneficial for heat-exchange devices and electrodes, where overheating and over-potential can be minimized.

4.3 Wetting in the Cassie–Baxter State

4.3.1 The Lotus Effect

When a liquid is in the Cassie–Baxter state on a rough surface, the droplet is usually characterized by a large contact angle with a small sliding angle. For water, the surface is designated as superhydrophobic. The most famous superhydrophobic surface is the Lotus leaf, exhibiting a water contact angle of 162° and a sliding angle of 4° [39]. During rolling off, dust and dirt particles adhere to the water droplet, resulting in the so-called self-cleaning effect. This observation has inspired numerous researchers worldwide and studies of superhydrophobicity have grown exponentially since. Fig. 4.17 shows the SEM micrographs of a leaf surface, which comprises micron-size aggregated wax crystals randomly distributed on the ~10–20 μm

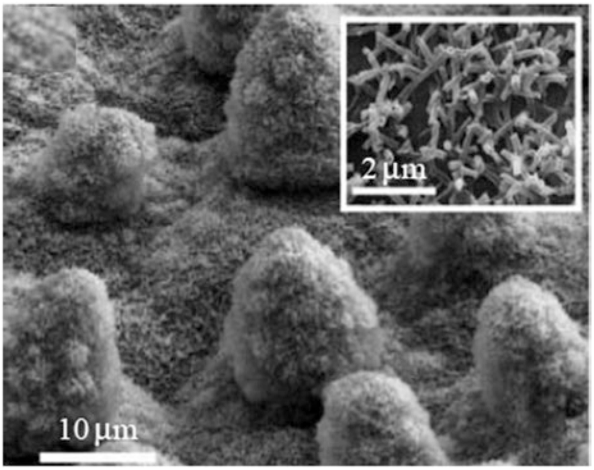

Fig. 4.17 SEM micrographs of the surface of a Lotus leaf (Reproduced from figures in [33], Copyright 2009 Elsevier)

papillae with the entire leaf surface carpeted with a layer of waxy nano-hairs (tubules) [32, 33, 39–41].

Tremendous attention has been paid to understand the hierarchical (multi-scale) surface structure and its effect on the super water repellency, hysteresis, wetting stability under pressure (e.g., against heavy raindrop), and mechanical properties [42–49]. Free energy analysis and thermodynamic modeling of hydrophobic surfaces suggest that a dual roughness scale (micron to submicron/nano) would result in large water contact angle, low contact angle hysteresis, and high wetting stability against the Cassie–Baxter to Wenzel transition. Theoretical calculations consistently reveal that a large contact angle is already achieved with a microscale surface and that the hierarchical structure is designed for low hysteresis and the ability to maintain the non-wetting state under high pressure. This is in agreement with experimental data [49]. More importantly, modellings also suggest that the micron-size feature is for mechanical stability of the surface [47]. The knowledge gained from nature has been very useful for the design and fabrication of artificial superhydrophobic surfaces.

The structure of the liquid–solid–air composite interface between water and the Lotus leaf was recently studied by Luo and co-workers using 3D confocal laser scanning microscopy, and the results are depicted in Fig. 4.18 [50]. With the bare leaf surface (Fig. 4.18a), a featureless rough dark surface is observed. Here, dark is indicative of solid surface. A very different image is observed for the interface. The image is bright indicative of reflective light by the trapped air. 3D roughness measurement of the composite interface suggests that the average thickness of the air cushion between the leaf surface and the water droplet is ~15 µm. This is inconsistent with the hierarchical structure shown in Fig. 4.17 and suggests that the main contact areas between water and the leaf surface are the tips of the papillae.

Although the chemical composition of plant wax has not been well characterized, Cheng and co-workers [40] found that the wax material on the Lotus is intrinsically, moderately hydrophilic with a water contact angle of 74°. As will be discussed in the next two sections, re-entrant structure and multi-scale roughness at

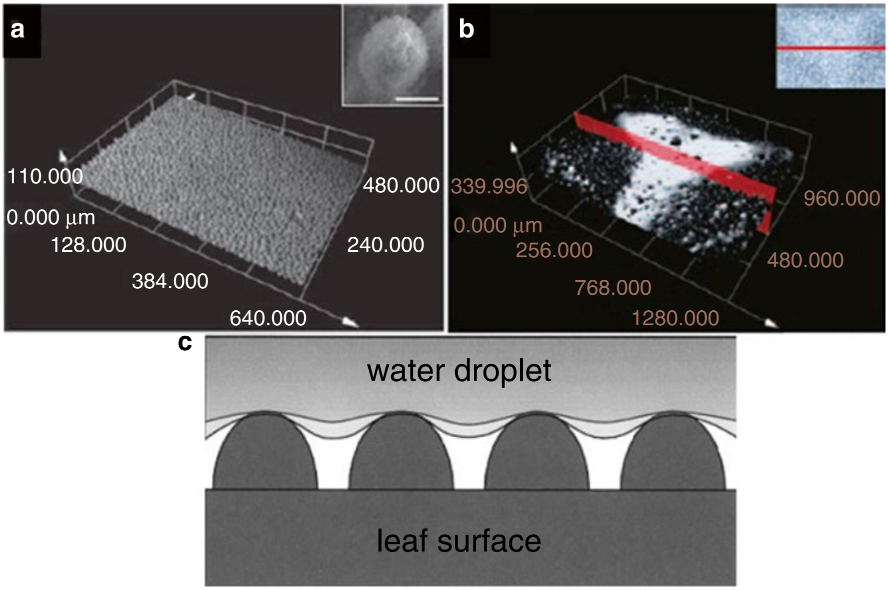

Fig. 4.18 Confocal laser scanning images of Lotus leaf (**a**) bare leaf (**b**) interface with a water drop, and (**c**) schematic of the interface from the image in (**b**) (Reproduced with permission from [50], Copyright 2010 Wiley)

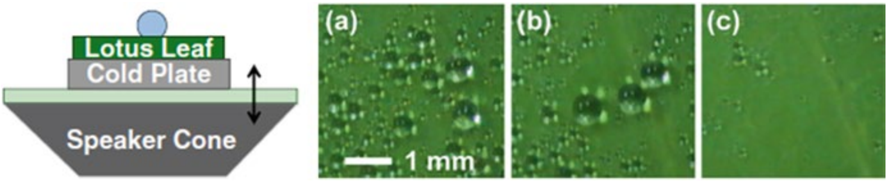

Fig. 4.19 Left: experimental setup for where the cold plate was used for the water condensation experiment; (**a**) condensation of water droplets on the Lotus leaf at cold plate temperature of 5 °C, (**b**) water droplets on horizontal Lotus leaf after titling (**a**) at 90°, and (**c**) water droplets on horizontal Lotus leaf after loudspeaker vibration of sample (**a**), followed by tilting the leaf to 90°. Most water droplets roll off after titling (Reproduced with permission from [53], Copyright 2009 American Physics Society)

the liquid–solid–air composite interface play critical roles in stabilizing the Cassie–Baxter state with moderately hydrophilic material. We believe that similar stabilization mechanism is operating when water wets the waxy tubules on the Lotus leaf [51]. The hydrophilic nature of the leaf surface is supported by water condensation experiments reported by Cheng and Rodak [52] and Boreyko and Chen [53]. Both groups showed that minute water droplets can condense on the Lotus leaf surface at high humidity. The experimental setup for the Boreyko and Chen experiment is given in Fig. 4.19. Basically, a fresh Lotus leaf is mounted onto a substrate under lab ambient condition of 21 °C at 50 % RH. The substrate is then cooled to 5 °C using a circulating bath. Minute water droplets were condensed and later coalesced into larger water droplets of ~2 mm in diameter (Fig. 4.19a). These drops are found to be in the Wenzel state as they are shown sticking on the Lotus surface when tilted to 90° (Fig. 4.19b). On the other hand, when these Wenzel drops are subjected to vibration noise from a loudspeaker (80 Hz, 1 mm peak-to-peak for 1 s), most water drops become mobile. They slide off the leaf surface upon tilting (Fig. 4.19c). This experiment indicate that, although the Cassie–Baxter state of the Lotus leaf is metastable, its energy level is fairly close to the most stable Wenzel state and can be populated by a simple vibration.

4.3.2 Artificial Superhydrophobic Surfaces

Inspired by the Lotus effect displayed in nature, there has been an exponential growth in research activity on superhydrophobicity [54, 55]. The consensus definition for a superhydrophobic surface is to have a water contact angle >150° and sliding angle $\approx 10°$ or less. This definition is somewhat arbitrary and a more refined definition has been published [56] and will be the subject of Chap. 6 in this book. Owing to the fascinating self-cleaning effect, superhydrophobic surfaces have been exploited for many potential applications, such as self-cleaning windows and textiles, oil- and soil-resistant clothing, anti-smudge surfaces for i-phone and display, anti-icing coatings for power line, roof-top and airplane, corrosion-resistant coatings for bridges and other metal structures, drag reduction in ship, gas and fuel transportation and microfluidic devices, etc. Numerous artificial superhydrophobic surfaces/coatings have been reported to date, and the subject has been reviewed frequently in recent literature (last 3 years) [57–62]. In this section, the focus will be on the key design parameters and wetting characteristics of these surfaces.

Based on the work of Wenzel and Cassie–Baxter [1, 2], the key parameters for superhydrophobicity are roughness and a hydrophobic surface coating. Roughness can be created by the top-down or bottom-up techniques or molding and embossing. Detailed descriptions of these processes have been reviewed in the literature and will not be detailed here. In the top-down approach, the roughness is created by etching a smooth surface with an energy (photons or electrons) beam or an etching agent, followed by modifying the surface with a hydrophobic coating if the material by itself is not hydrophobic. Significant efforts have been on pillar array surfaces, where the effects of surface chemistry and roughness on contact angle, hysteresis, and wetting stability in terms of the Cassie–Baxter-to-Wenzel transition have been investigated [63–66]. In pillar array surface, roughness and solid-area fraction are controlled by the pillar dimension and geometry, length scale, and pillar height. These surfaces are usually fabricated by lithographic technique or e-beam etching followed by surface hydrophobization with an alkysilane or a perfluoroalkysilane. In 2009, Byun and co-workers reported the preparation of 5×5 μm square pillar (height = 5 μm) array surfaces of varying pitch to model the wettability of insect wings [66]. The model surfaces were prepared by photolithography on silicon wafer and the final textures were surface modified with a fluorosilane layer FOTS, a fluorinated self-assembled-monolayer synthesized from tridecafluoro-1,1,2,2-

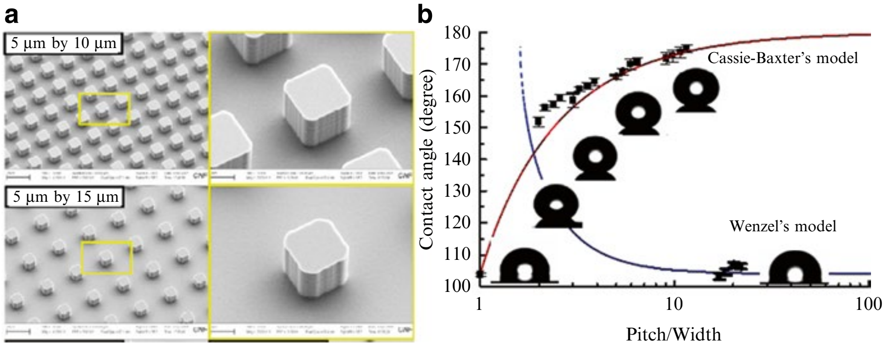

Fig. 4.20 (**a**) Representative SEM micrographs of square pillar array FOTS surfaces and (**b**) plot of water contact angle as a function of pitch/width ratio of the pillar array surface (Reproduced with permission from [66], Copyright 2009 Elsevier)

tetrahydrooctyltrichlorosilane. Representative SEM micrographs of the surfaces are given in Fig. 4.20a. The water contact angles of the model surfaces are plotted as a function of the pitch/width ratio (Fig. 4.20b). Results show that contact angle increase as pitch/width ratio increases initially. At pitch/width ratio between 2 and 15, large contact angles which are predicted by the Cassie–Baxter model are observed, indicating that these surfaces are superhydrophobic. Transition occurs at pitch/width ≈ 15. Water droplets are in the Wenzel state when pitch/width is ≥20, indicating that the sagging water interface touches bottom of the pillar array surface. The entire surface becomes fully wetted as a result.

Very similar results were also reported by Oner and McCarthy [63], who found that their 8 × 8 µm square pillar array surface (height 40 µm) was in the Wenzel state when the pitch is ≥56 µm. For 8 × 8 µm square pillar array with pitches ≤32 µm, $\boldsymbol{\theta}_A$ is essentially constant at ~174°. On the other hand, $\boldsymbol{\theta}_R$ is shown to decrease as the pitch decreases. The result is attributed to the increase in contact line length per unit area. Water pins at the edge of the pillar top, the smaller the pitch, the longer the contact line per unit area, the smaller the $\boldsymbol{\theta}_R$. This interpretation is supported by studying the $\boldsymbol{\theta}_R$ values of pillar array surface with different pillar geometry.

For the bottom-up approach, the rough surface can be created by polymerization of a monomer via plasma-enhanced CVD technique or electropolymerization. Surface morphology is sensitive to the polymerization condition. Usually, the roughness is random with a hierarchical particulate or fibrous structure. When a hydrophobic monomer is used, the surface will be superhydrophobic after polymerization. Figure 4.21a shows a 10 × 10 µm AFM image of a PECVD polymer film polymerized from perfluorooctyl acrylate. The surface comprises nanospherical particles and exhibits very high water repellency with $\boldsymbol{\theta}_A/\boldsymbol{\theta}_R$ at 168°/165° [67]. Similarly, electropolymerization of 3,4-ethyleneoxythiathiophene derivatives also yield superhydropho-

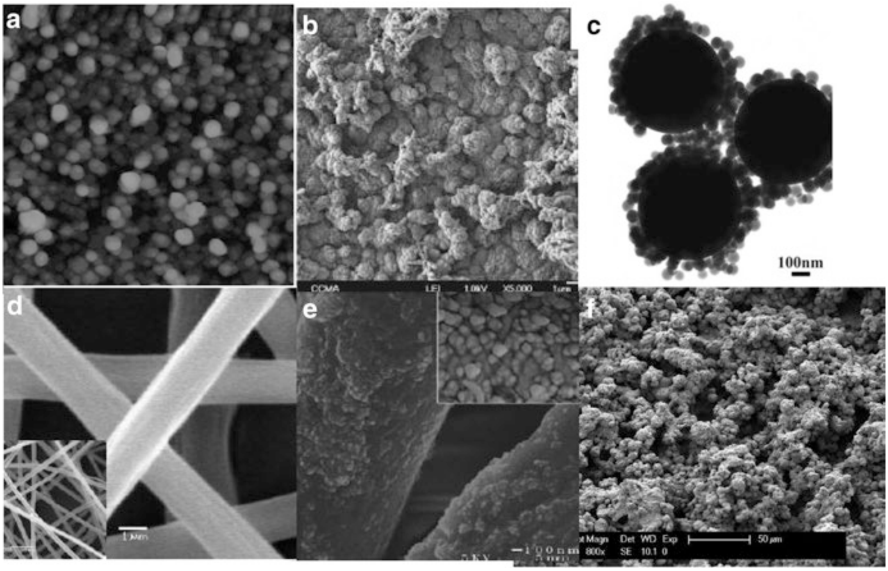

Fig. 4.21 Mosaic of rough superhydrophobic surfaces prepared by different techniques (**a**) PECVD, (**b**) electropolymerization, (**c**) grafting by amine-epoxy reaction, (**d**) electrospinning, (**e**) electrospinning plus layer-by-layer, and (**f**) spray

bic surfaces with $\boldsymbol{\theta}_{\mathrm{A}}$ ~160° and low hysteresis. The surface morphology varies from particulate to fibrous and an example is given in Fig. 4.21b [68].

Other popular bottom-up approaches to build rough surfaces include the uses of silica particles or micro/nanofibers from electrospinning [69] or simply spraying a particle-polymer solution onto a substrate. Ming and co-workers [70] reported the preparation of dual scale rough epoxy surface consisting of raspberry-like particles. A schematic for the preparation of the silica-epoxy film is given in Fig. 4.22. First, the raspberry-like particles are prepared by grafting 70 nm amine-functionalized silica particles onto the larger 700 nm epoxy-functionalized silica particles. A TEM micrograph of the raspberry-like silica particles is given in Fig. 4.21c. The superhydrophobic surface is created by grafting the raspberry particles onto an epoxy substrate followed by hydrophobization of the hierarchical surface with a silicone material. The resulting surface was shown to exhibit a $\boldsymbol{\theta}_{\mathrm{A}}$ of 165° with a 3° roll-off angle. Ma et al. [71] prepared fiber mat of diameter of ~1.7 µm with average pore size of 80 nm using the electrospinning technique (Fig. 4.21d). After hydrophobization of the fiber mat with a fluoropolymer, the resulting fiber mat is superhydrophobic with $\boldsymbol{\theta}$ at ~150°. Fiber mats with hierarchical multi-scale roughness, such as by creating nano pores on the fiber surface or the use of layer-by-layer technique to decorate the electrospun fiber with nano silica particle (Fig. 4.21e), are known to further enhance the water repellency [71]. Spray is a scalable technique that can coat large surface area of different geometry. Steele and co-workers applied the technique to prepare nanocomposite coatings containing 50 nm ZnO nanoparticles

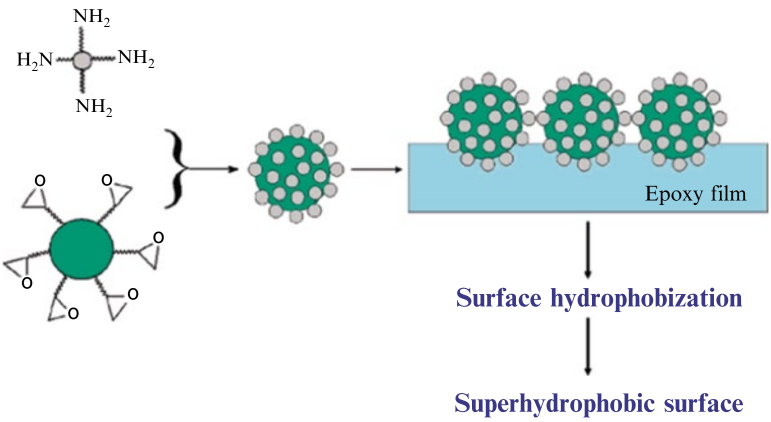

Fig. 4.22 A schematic for the preparation of raspberry-like particles and a superhydrophobic surface with multi-scale roughness (Reproduced with permission from [70], Copyright 2005 The American Chemical Society)

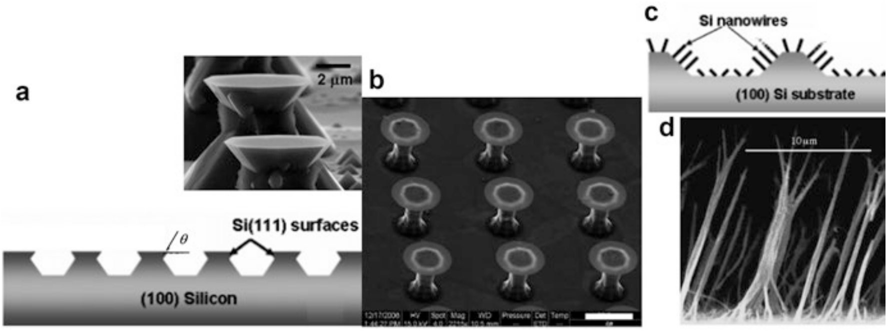

Fig. 4.23 Mosaic of superhydrophobic surfaces prepared with moderately hydrophilic materials/surfaces (**a**) silicon, (**b**) DLC coating (scale bar 20 μm), (**c**) silicon nanowire, and (**d**) poly(vinyl alcohol) nanofibers (scale bar 10 μm)

and a waterborne perfluoroacrylic polymer on a substrate [72]. The resulting surface comprises a hierarchical roughness structure (Fig. 4.21f) and exhibits superhydrophobic property (water $\boldsymbol{\theta} > 150°$ with low hysteresis).

One of the less recognized approaches to design superhydrophobic surface is the use of re-entrant/overhang structure or very low solid-area fraction at the composite interface. Because of the high water surface tension, superhydrophobicity can be attained with moderately hydrophilic materials. Using photolithography, Cao et al. [51] fabricated a pillar array surface with an overhang on silicon wafer (Fig. 4.23a). Since no extra coating is used, the surface of the textured surface is basically hydrogen-terminated silicon which has a contact angle of 74°. The water contact angles of the textured surfaces range between 150 and 160° at solid-area fraction ≤ 0.07. Similarly, Wang et al. [73] created superhydrophobic surfaces with T-shape pillars on silicon wafer followed by coating the textured surfaces with a ~100 nm thick diamond-like-carbon (DLC) film (Fig. 4.23b). While the water contact angle of a smooth DLC film is at ~72° and the textured surfaces exhibit superhydrophobic-like contact angles at ~160°. Superhydrophobic surface can also be fabricated with hydrophilic materials at very low solid-area fraction. For example, in the Cao et al. study [51], they also fabricated a rough, multi-scale surface by decorating the silicon bumps with Si nanowires (Fig. 4.23c). Again, native silicon is hydrophilic but very large contact angle (~160°) was obtained. Similarly, Feng and co-workers [74] were able to grow a poly(vinyl alcohol) (PVA) nanofiber forest (Fig. 4.23d) using an aluminum oxide template and observed an apparent water contact angle of 171°. PVA is a hydrophilic polymer with known water contact angle at ~72°. The commonality of the latter two surfaces is that they all have very low solid-area fraction. Even though water is pinned at the tip of the nanowire or fiber, the close proximity of the pinning location, coupled with the high water surface tension, enables air pockets to be formed and superhydrophobicity. In summary, the design rules for superhydrophobicity are: chemistry, roughness, and re-entrant structure or very low solid-area fraction. The very low solid-area fraction can be achieved using a hierarchical textured approach or a nanowire or nanoforest approach. The above studies also indicate that meeting two out of three requirements will be sufficient for superhydrophobicity. We however suggest that meeting all three requirements would be beneficial from the viewpoints of improving the robustness of the superhydrophobic state as well as increasing its resistance to collapse under high external pressure.

4.3.3 Cassie–Baxter to Wenzel State Transition

It has been known for some time that micro/nano rough surfaces can exist in both Cassie–Baxter and Wenzel wetting states depending on the experimental conditions. For example, He and co-workers [75] showed that water droplet is in the Cassie–Baxter state on the PDMS microtextured surface if the drop is dispensed gently. On the other hand, a Wenzel droplet is obtained when the drop is dispensed at some height. Photographs of these two droplets are reproduced in Fig. 4.24. The results clearly indicate that the Wenzel droplet is the more stable state. In a slightly different experiment, Quere et al. [76, 77] created a Cassie–Baxter droplet with $\boldsymbol{\theta}_\mathrm{A}$ of 163° on a fluorinated microtextured surface. This Cassie droplet can be converted to the Wenzel droplet when an external pressure is applied. A similar Wenzel droplet can also be created on the same surface by a condensation experiment. While Bormashenko and team [78, 79] showed that the Cassie water droplet can be de-pinned and formed the Wenzel droplet via vibration noise, Boreyko and Chen [53] on the other hand demonstrated that the Wenzel drops obtained by condensing water on the Lotus leaf at high humidity can be converted to the Cassie droplet by vibration too! Another example of "exciting" the Wenzel droplet to the Cassie droplet is provided by Liu and co-workers [80] who were able to turn a Wenzel droplet to

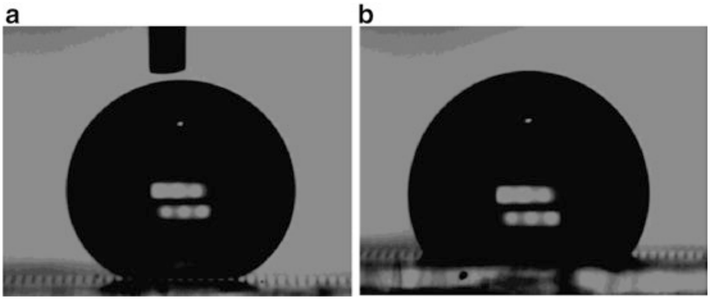

Fig. 4.24 Photographs of (**a**) Cassie and (**b**) Wenzel water droplet obtained on the same microtextured PDMS surface (Reproduced with permission from [75], Copyright 2003 The American Chemical Society)

the Cassie droplet by heating. The overall results seem to suggest that although the Wenzel state may be more stable, the fact that they are interconvertible depending on the experimental condition implies that (1) there exists an energy barrier between them and (2) their difference in energetics is probably small.

In most practical applications, surfaces with high water repellency and self-cleaning property are desired. Approaches to enhance the stability of the Cassie–Baxter state include increase the energy barrier between these states or better yet stabilize and make Cassie–Baxter state the more stable state. Both theoretical analysis and experimental results [81–85] indicate that having a hierarchical, multi-scale roughness structure, a re-entrant structure, along with a hydrophobic surface coating would increase the energy barrier between the Cassie–Baxter and Wenzel state. The increase of barrier height not only enhances the stability of the metastable Cassie–Baxter state, it will also increase its resistance to collapse against external pressure. Moreover, there is preliminary indication that, under certain hierarchical roughness structure, the Cassie–Baxter state may be more favorable thermodynamically [84, 85].

4.3.4 Superoleophobicity

The surface tension of hydrocarbon oil is a lot lower than water. Hexadecane has frequently been used as the probing liquid for oleophobicity, and its surface tension is almost three times lower than that of water (27.5 vs. 72.3 mN/m). It wets most surfaces as a result. Even more challenging is that smooth surface with hexadecane $\theta > 90°$ is not known. Thus, surface with super hexadecane repellency is rare. The consensus definition for superoleophobicity is surface exhibiting hexadecane contact angle >150° and sliding angle ~10°. Unlike superhydrophobic surface, which can be superoleophilic [86, 87], superoleophobic surface is expected to be more versatile as it will repel most liquids ranging from water to alkanes.

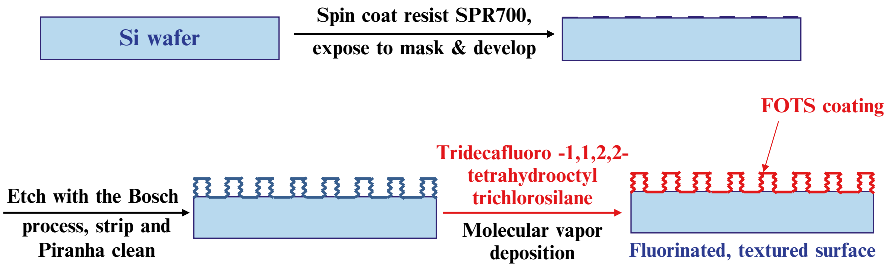

Fig. 4.25 Schematic for the fabrication of fluorinated surface texture on silicon wafer (Reproduced with permission from [88], Copyright 2011 The American Chemical Society)

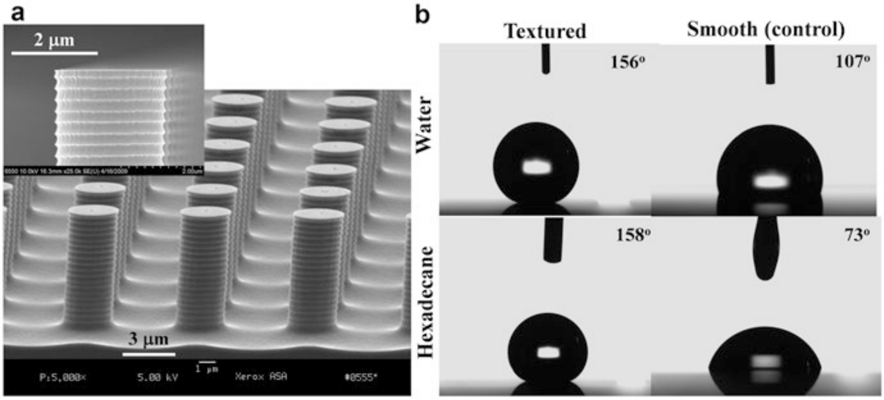

Fig. 4.26 (**a**) SEM micrograph of the textured FOTS surface on Si-wafer (inset: higher magnification micrograph showing details of the pillar structure) and (**b**) static contact angles for water and hexadecane on the textured FOTS surface (control: smooth FOTS surface on Si-wafer) (Reproduced with permission from [88], Copyright 2011 The American Chemical Society)

To elucidate the basic design parameters for superoleophobicity, Zhao et al. [88] launched a systematic investigation using model pillar array surface with well-defined texture and geometry. Figure 4.25 summarizes the surface texturing and chemical modification procedure for the fabrication of the model textured surface. Details of the fabrication processes have been published elsewhere [88].

Figure 4.26a shows the SEM micrograph of the FOTS pillar array surface, comprising ~3 µm diameter pillar arrays ~7.8 µm in height with a pitch of ~6 µm. High magnification SEM micrograph (insert) reveals that the sidewall in each pillar consists of a ~300 nm wavy structure from top to bottom, attributable to the Bosch etching process. The surface property of the FOTS pillar array surface was studied by both static and dynamic contact angle measurement techniques and the static contact angle data with water and hexadecane as test liquids are given in Fig. 4.26b. The water and hexadecane contact angles for the FOTS pillar array surface are at 156° and 158°, respectively, and are significantly higher than those of the controlled smooth surfaces, which are at 107° and 73°, respectively. The results suggest that the high contact angles observed for the FOTS pillar array surface are the result of both surface texturing and fluorination. The sliding angles for the FOTS pillar array surface are found to be ~10° with both water and hexadecane. The high contact angles coupled with the low sliding angles lead to the conclusion that the FOTS pillar array surface is both superhydrophobic and superoleophobic with low hysteresis.

The use of photolithography and hydrophobic coatings to create micro/nano textured surfaces is not new [63–66]. The sidewalls of all the reported pillar structures were smooth, and only superhydrophobicity was reported, not superoleophobicity. Recently, Tuteja and co-workers [89] reported the fabrication of electrospun mats that exhibited superoleophobicity. The mat comprises nanofibers made from F-POSS (*1H,1H,2H,2H*-heptadecafluorodecyl polyhedral oligomeric silsesquioxane) and PMMA (poly(methyl methacrylate)) blends. The flat surface of the same material is oleophilic with a hexadecane advancing contact angle of ~80°. To elucidate the mechanism for the superoleophobicity of the electrospun mat, these authors created the so-called micro hoodoo structure on silicon wafer using photolithography and surface fluorination. These authors concluded that the re-entrant geometry in the "micro-hoodoo" structure is critical to achieving superoleophobicity and the electrospun mat has a similar geometry at the liquid–solid–air composite interface. The conclusion is substantiated by additional experimental and modeling studies [86, 87, 90].

To elucidate the origin for the observed superoleophobicity, FOTS pillar array surfaces with (a) a smooth straight sidewall and (b) a straight sidewall with an overhang structure were fabricated (Fig. 4.27). The wetting properties with water and hexadecane were examined and key sessile drop data are included in the figure. The

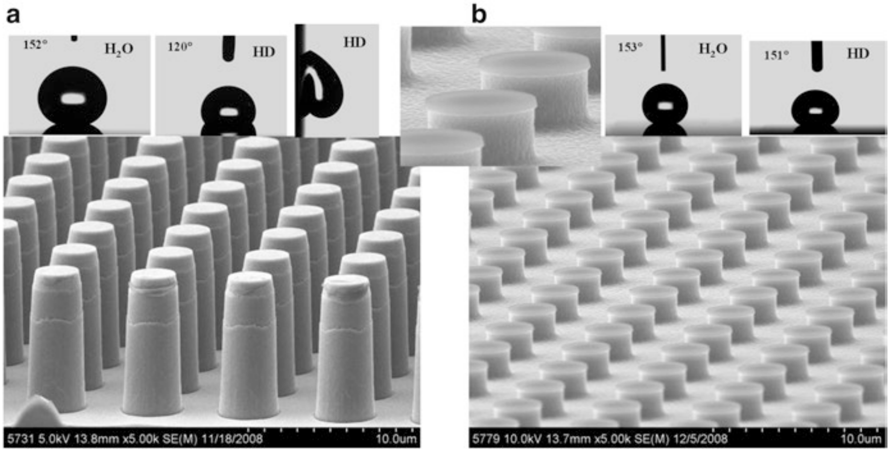

Fig. 4.27 (**a**) SEM micrograph of the textured FOTS surface with straight smooth sidewall pillars on Si-wafer; and (**b**) SEM micrograph of the textured FOTS surface with an overhang pillar structure on Si-wafer (insert: sessile drop data for water and hexadecane on the textured surfaces) (Reproduced with permission from [88], Copyright 2011 The American Chemical Society)

results show that both surfaces are superhydrophobic, but that there is a significant difference in oleophobicity. For pillar array surface with a smooth, straight sidewall, the hexadecane drop exhibits a hexadecane contact angle of 121°, but the drop was found stuck on the surface when tilt to 90°. On the other hand, the surface with an overhang pillar was shown to be superoleophobic with hexadecane contact angle and sliding angle at 150° and 12°, respectively. The similarity in wetting properties between the model surface with the wavy sidewall and the pillar surface with the overhang structure leads to the conclusion that the re-entrant structure at the top of the wavy sidewall is a key contributor to the superoleophobic property. This conclusion is not only in agreement with those reported by Tuteja and co-workers [86, 87, 89, 90], but also consistent with other observations reported by Fujii et al. [91], Cao et al. [92], Ahuja et al. [93], and Kumar and co-workers [94]. They all pointed to the importance of the re-entrant or overhang structure in achieving surface superoleophobicity. Hence, the basic parameters for superoleophobicity are: chemistry (contact angle of the coating), roughness, and re-entrant geometry. Unlike superhydrophobicity where meeting two out of three requirements is sufficient, superoleophobicity demands all three requirements attributable to the lowering of the surface tension of the probing liquid.

An attempt was made to visualize the composite interface using hot polyethylene wax. Figure 4.28a shows the image of a hot polyethylene wax sessile droplet on the model pillar array surface at 110°C. The contact angle and the sliding angle of the droplet were measured at 155° and 33°, respectively, consistent with the hexadecane data. The data suggests that the wax droplet is in the Cassie–Baxter state on the pillar array surface (Fig. 4.28b). When the wax droplet was cooled to room temperature, it was carefully detached from the textured surface and the geometry of the composite interface was examined by SEM microscopy. Figure 4.28c shows the

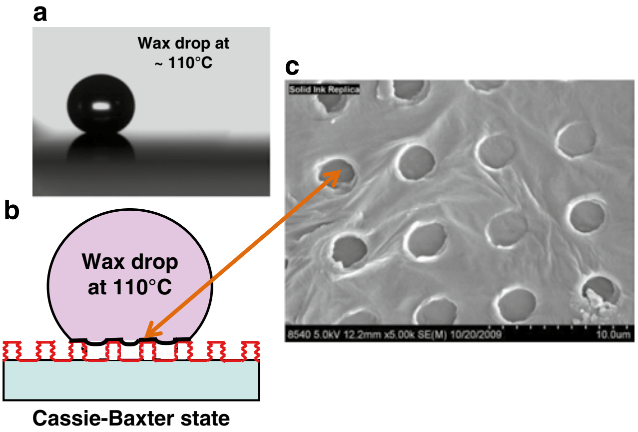

Fig. 4.28 (**a**) Molten droplet of polyethylene wax on the pillar array surface, (**b**) wax droplet in the Cassie–Baxter sate, and (**c**) SEM micrograph of the wax replica of the composite interface after the wax droplet is cooled to room temperature (Reproduced with permission from [88], Copyright 2011 The American Chemical Society)

SEM micrograph of the liquid–solid–air composite interface. The result indicates that the wax surface is "flat" with holes corresponding to the location of the pillars. From the thickness of the "rim," one can estimate the penetration depth of the molten wax droplet into the void space between the pillars, which is <0.5 μm. Since the height of the pillar is ~7 μm, this result positively reveals that the molten wax droplet is indeed sitting on air at the interface of the superoleophobic surface. However, the composite interface is not perfectly flat; the molten wax appears to penetrate into the void space between the pillars. Although the composite interface for water on the FOTS pillar array surface was not imaged, we believe that the water droplet is in the Cassie–Baxter state too based on the contact angle and sliding angle data.

The effect of surface texturing, including pillar pitch, diameter and height, on both static and dynamic contact angles have also been studied [95]. The contact angle results ($\boldsymbol{\theta}_{\mathrm{A}}$, $\boldsymbol{\theta}_{\mathrm{R}}$, $\boldsymbol{\alpha}$, and hysteresis) are plotted as a function of solid-area fraction and are summarized in Fig. 4.29. The results show that surface texturing has very little effect on the static and advancing contact angles for both water and hexadecane. On the other hand, pillar spacing has profound effects on the dynamic contact angles, particularly the sliding angle, the receding contact angle and the contact angle hysteresis. $\boldsymbol{\theta}_{\mathrm{R}}$ decreases, and $\boldsymbol{\alpha}$ and ($\boldsymbol{\theta}_{\mathrm{A}}$–$\boldsymbol{\theta}_{\mathrm{R}}$) increase for both water and hexadecane, indicating that surface adhesion increases and drop mobility decreases as the solid-area fraction increases. This is attributed to the pinning of the liquid droplet on the pillars, the larger the solid-area fraction the more the pinning sites (or the higher the contact line density). It is important to point out that the effect of solid-area fraction is larger for hexadecane, and this is due to their difference in the pinning location [95].

Also included in Fig. 4.29a, b are results from pillar array surfaces with 1 and 5 μm diameter pillars (represented by data points X and O, respectively). These data points are completely compatible with the results of the 3 μm pillar array surfaces, indicating that surface adhesion and drop mobility are governed primarily by the density of the contact lines, not the geometry of the texture.

The effect of pillar height on the superoleophobic properties was studied using 3 μm pillar array surfaces with a center-to-center spacing of 12 μm. This pillar spacing is wider than the surface shown in Fig. 4.26 and represents a more stressful case for liquid sagging. The pillar height was controlled by the number of Bosch-etching cycles and is varied from about ~0.8 to 8 μm. Figure 4.30 shows the SEM micrographs of three representative surfaces along with the plots of contact angle data against the pillar height for both water and hexadecane. The results show that pillar array surfaces can maintain its Cassie–Baxter state with both water and hexadecane as long as the pillar height is >1 μm. For surfaces with pillar height ≤0.8 μm, both water and hexadecane droplets are unstable. They are shown to wet the entire surface sooner or later. This indicates that the liquid droplets sag and touch the bottom of the surface fully wetting it as a result. To avoid wetting transition from the Cassie–Baxter to Wenzel state, pillar height should be >1 μm.

In summary, we show with model pillar array surfaces that hydrocarbon oils can trap air pockets on rough surfaces and result in a Cassie–Baxter composite interface when the following basic parameters are met: high hexadecane contact angle surface

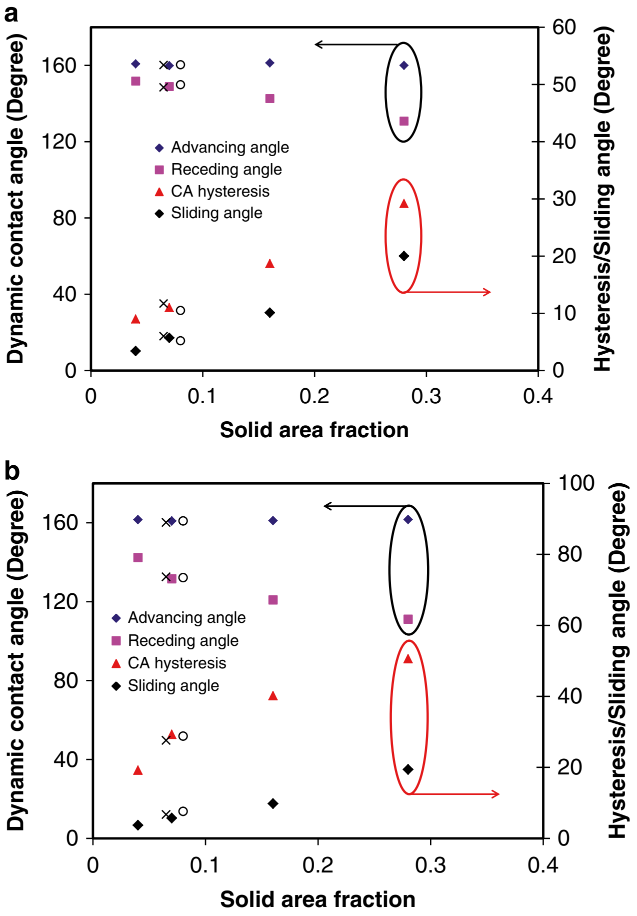

Fig. 4.29 Plots of dynamic contact angle data with (**a**) water and (**b**) hexadecane versus solid-area fraction for 3 μm pillar array surfaces. (*Insert*: dynamic contact angle data from a 1 μm pillar array (X) and a 5 μm pillar array (O) surface) (Modified from figures in [95], Copyright 2012 The American Chemical Society)

coating and a rough surface with an overhang or re-entrant structure. Since oleophobic coating does not exist, the re-entrant structures, which allow the hydrocarbon liquid to pin at the composite interface is essential in achieving superoleophobicity.

4.4 Directional Wetting and Spreading

In most rough surfaces, whether the texture is patterned regularly or randomly, wetting and spreading on them are isotropic two dimensionally. However, if the texture or roughness is created with different wettability directionally, anisotropic wetting and spreading will occur. This happens in nature as well as artificial surfaces. Two famous examples in nature are the groove structures in the wings of butterfly [96] and the directional papillae array structure in rice leaf [97]. Figure 4.31a depicts a picture of an iridescent blue butterfly. The SEM micrograph of the wing (Fig. 4.31b) shows that the wing comprises layers of "leaves" stacking outward

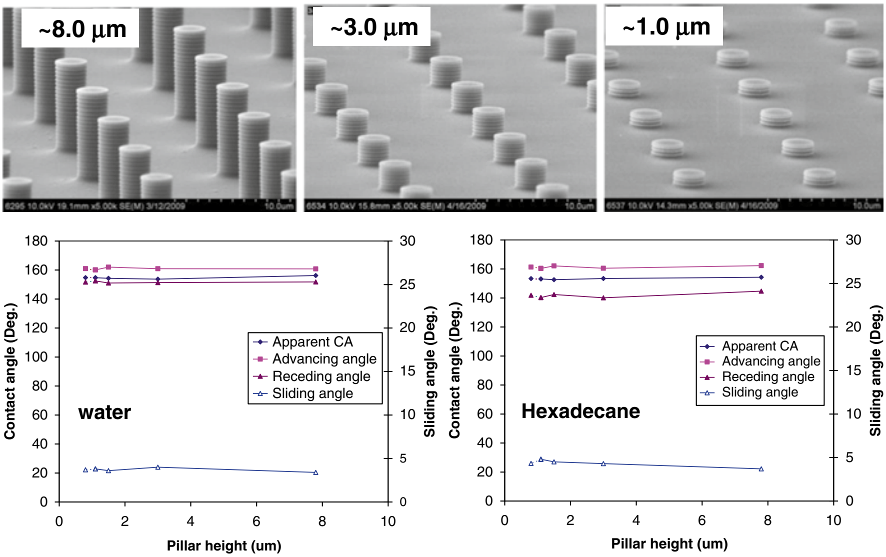

Fig. 4.30 (*top*) SEM micrographs of 3 μm pillar array surfaces with different height and (*bottom*) plots of static and dynamic contact angles of the 3 μm pillar array surfaces as a function of pillar height

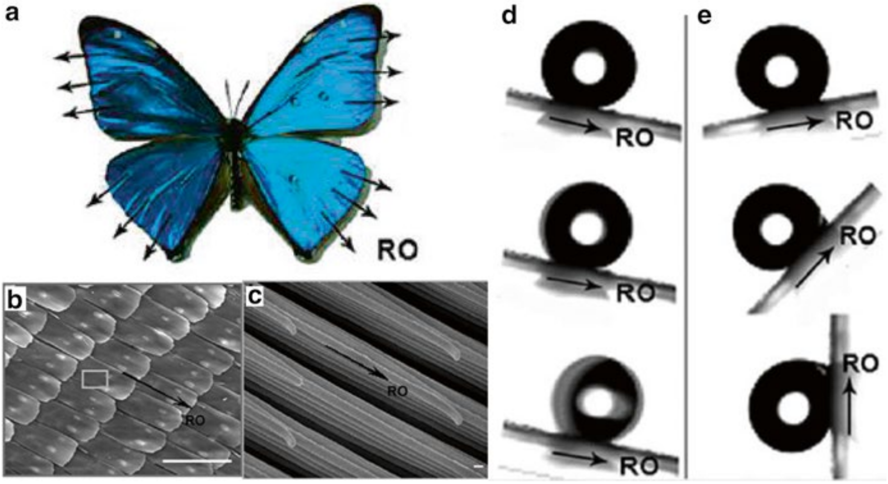

Fig. 4.31 (**a**) Photograph of an iridescent blue butterfly, (**b**) SEM micrograph of the wing of butterfly, scale bar 100 μm, (**c**) high magnification SEM micrograph of the wing of butterfly, scale bar 100 nm, and (**d**, **e**) water sessile drop data in outward and inward direction, respectively (Reproduced with permission from Ref. 96, Copyright 2007 The Royal Society of Chemistry)

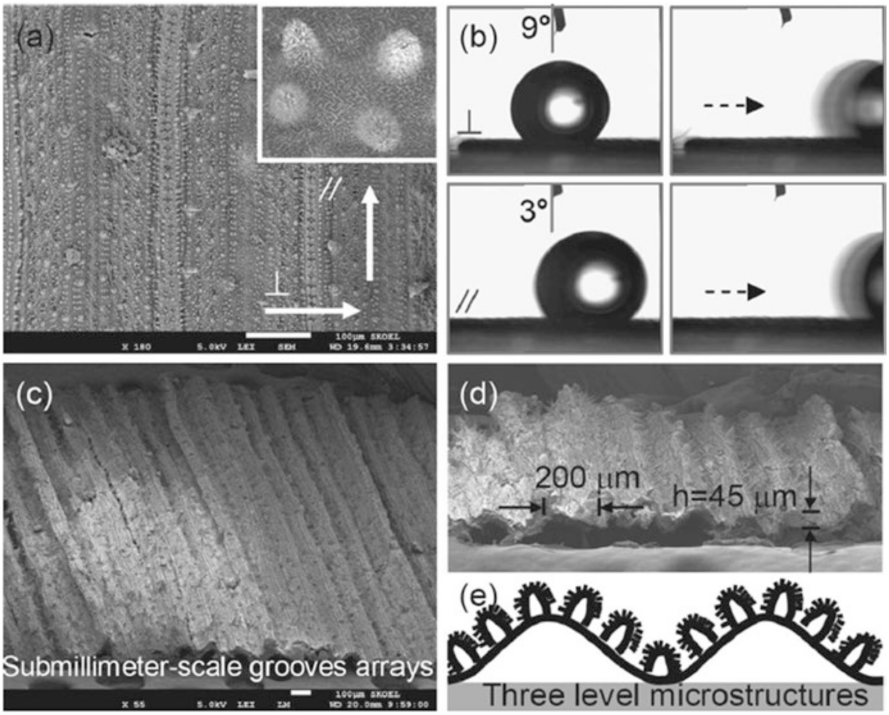

Fig. 4.32 (**a**) SEM micrograph of a rice leaf, scale bar 100 µm, (inset: highly magnified SEM), (**b**) water sessile drop data on the leaf surface, (**c**) SEM micrograph at 60° tilt angle, scale bar 100 µm, (**d**) cross-section SEM micrograph, and (**e**) a schematic of the hierarchical surface structure of the rice leaf. (Reproduced with permission from Ref. 97, Copyright 2011 Wiley)

orderly. High resolution SEM micrograph (Fig. 4.31c) further reveals that the leaves are made of groove structure in both micron and nanoscales. This dual scale structure facilitates air-trapping when contact with water. On the top of that, each leaf also comprises a couple of nano hooks with the tips curving inward. Due to the hierarchical roughness, the measured water contact angle for the butterfly wing is at ~152°. The most interesting property is its directional wetting property. When the wing is tilting downward, water droplet is able to slide freely along the RO direction (Fig. 4.31d). On the other hand, when the ring is tilting upward, the water droplet is shown stuck on the wing surface even when it is tilted to 90° (Fig. 4.31e). This is attributable to the frictions created by the nano hooks as well as the edge of the leaves in the against direction. Undoubtedly, after millions of years of evolution, this is one of the ways the butterfly tries to keep itself dry in the rain.

Figure 4.32 summarizes results from the SEM microscopy studies of the rice leaf along with water sessile drop data [97]. In terms of surface texture, rice leaf exhibits submillimeter groove structure with width at ~200 µm and height ~45 µm (Fig. 4.32c, d). Each groove is made of micron-size papillae array lining up in the direction of the groove, and the entire surface is covered with nano-size hairy plant wax (Fig. 4.32a). This hierarchical surface structure has resulted in a very large water contact angle (~150°). Due to directionality of the papillae arrangement, water droplet displays anisotropic sliding angle. Specifically, the sliding angles were found to be 3° and 9° in the parallel and perpendicular direction, respectively. As a surface design, the superhydrophobic nature of rice leaf leads to self-cleaning, ensuring efficient absorption of the sunlight for photosynthesis during the growing season. At the same time, the directional water sliding will make sure water and nutrient are delivering to the root effectively, again for growth and survival.

Mimicking nature, many artificial groove structured surfaces ranging from micron to nano length scale of varying hydrophobicity have been reported [98–101]. Typically, the droplet is elongated. The distortion is a function of the geometry of the groove (width and spacing), the drop size, and the wettability of the surface. Figure 4.33a shows a schematic for a series of 3 μm deep, PMMA groove surfaces with width (spacing) varying from 5, 10, 25, 50, to 100 μm. These surfaces were made by the hot embossing technique with appropriate lithographically prepared silicon molds [101]. After molding, the surfaces were modified by a plasma polymerized coating. The wettability of the surface coating is controlled by the type of monomer used. Two monomers, namely allylamine and hexane were used and they provide a hydrophilic

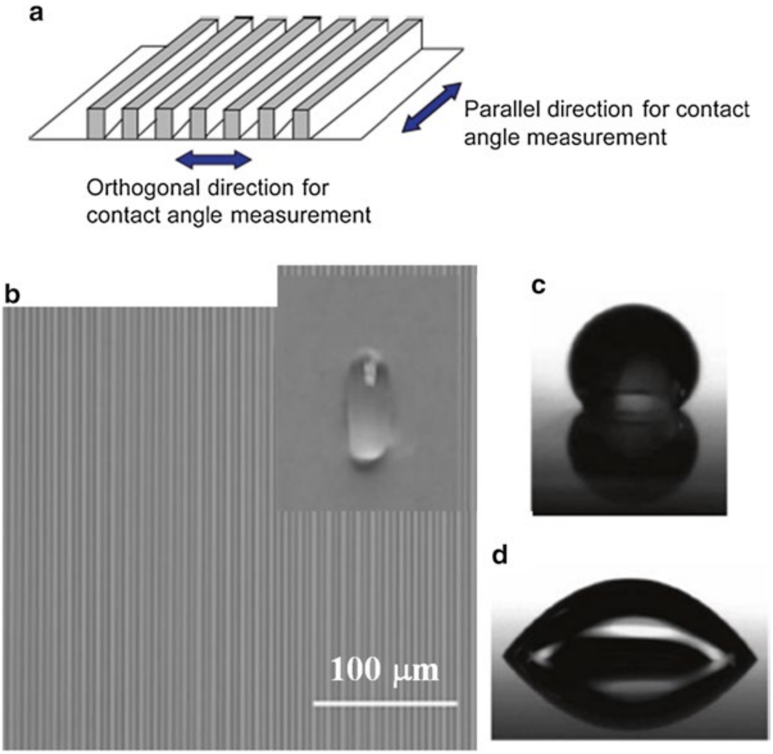

Fig. 4.33 (**a**) A schematic of the groove PMMA surface, (**b**) optical image of a 5 μm groove surface, and (**c**, **d**) sessile drop data on the surface in the perpendicular and parallel direction (Reproduced with permission from [101], Copyright 2009 The American Chemical Society)

and hydrophobic surface coating with water contact angles at ~60° and ~98°, respectively. Figure 4.33b shows a photograph of a typical surface and the shape of the water sessile droplet is given in the insert. Figure 4.33c, d show the water sessile drop data in the perpendicular and parallel direction, respectively. It is clear that the water droplet is elongated in the parallel direction due to wetting interaction between water and the groove surface. The contact angle in the perpendicular direction is always larger than that in the parallel direction.

Yang et al. [101] went on to investigate the effects of groove width, drop size, and coating chemistry on the wettability of the groove surfaces. The water contact angle data, by plotting the contact angles as a function of the chemistry in the perpendicular and parallel direction, are summarized in Fig. 4.34a, b. The upper and lower dash lines in the plots are the calculated Cassie–Baxter and Wenzel angles, respectively, based on the surface chemistry and texture geometry. Not unexpectedly, there is little agreement between the calculated Cassie–Baxter/Wenzel angles with the experimental values. For groove surfaces with the hydrophilic coating, they are expected to be in the fully wetted by water. The results in Fig. 4.34a clearly show that (1) the parallel direction is more wettable (smaller contact angle) than the perpendicular direction, and (2) the distortion of the drop increases as the size of the water droplet increases. While increase of drop size has little effect on the contact angle in the parallel direction, the effect in the perpendicular direction is much larger. In fact, this effect is the prime contributor to the drop size effect on drop elongation. The observation is attributed to the difference in wettability between the parallel and perpendicular direction. When the water drop is spreading in the parallel direction, there is little change in solid-area fraction, always 50 %. On the other

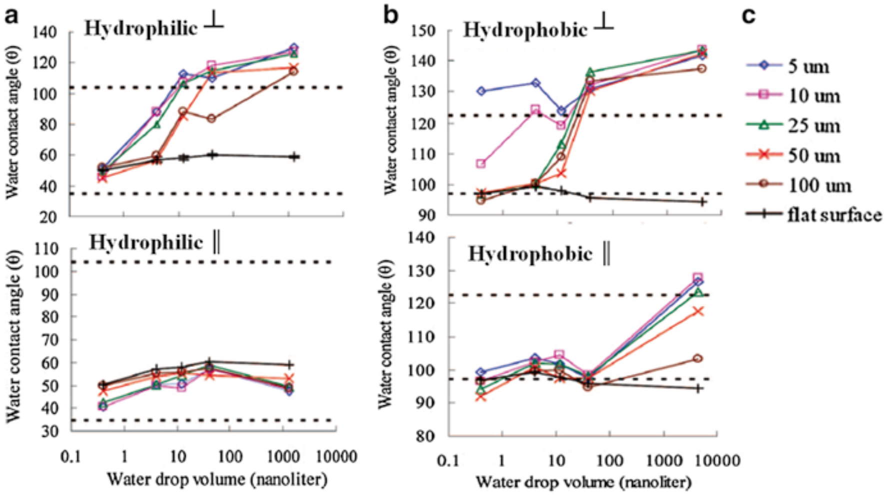

Fig. 4.34 Plot of water contact data as a function of the drop size for (**a**) hydrophilic coated and (**b**) hydrophobic coated PMMA groove surfaces (*top*: measured in the perpendicular direction, *bottom*: measured in the parallel direction), and (**c**) width of the grooves in (**a**) and (**b**) (Modified from [101], Copyright 2009 The American Chemical Society)

hand, as the contact line is advancing perpendicularly, it is experiencing friction due to pinning at the edge of the groove 50 % of the time, the larger the drop size, the more friction the drop experiences during advancing. The largest retardation to contact line advance is expected for groove surface with the narrowest width (5 μm). Indeed, the largest water contact angle is observed for the 5 μm groove surface in the perpendicular direction.

With the hydrophobic coating (Fig. 4.34b), the groove surface can be in the Wenzel or Cassie–Baxter state depending on the drop size. Although anisotropic wettability is observed, there is no clear trend between drop elongation and drop size as the case for the hydrophilic groove surfaces. From the size of the contact angle, it appears that water droplet is in the Cassie–Baxter state when the droplet is >50 nL. The droplet appears to be in the Wenzel state for the 0.5 nL drop and then transitioning to the Cassie–Baxter state as the drop size increases.

Directional self-cleaning superoleophobic groove surface was reported by Zhao and Law in 2012 [102]. The surface, prepared by photolithographic technique followed by surface fluorination, comprises 4 μm deep, 3 μm wide groove structure with a 6 μm pitch. Figure 4.35a shows the SEM micrograph of the groove surface. Due to the Bosch etching process, wavy sidewall similar to those in the pillar array surface was obtained. The water and hexadecane sessile drop data are summarized in Fig. 4.35b, and anisotropic wettability is evident for both liquids. The contact angles in the orthogonal direction for water and hexadecane are at 154° and 162°, respectively, and are consistently larger than those in the parallel direction, which are at 131° and 113°, respectively. The large contact angles suggest that both liquids are in the Cassie–Baxter state on the groove surface. Interestingly, the sliding angles for water and hexadecane are found to be smaller in the parallel direction, 8° and 4° as compared to 23° and 34° in the orthogonal direction, despite having smaller contact angles. The overall wetting data can be rationalized based on the pinning effect. For example, due to the friction created at the edge of the sidewall, liquid advance in the orthogonal direction will be retarded every time the liquid advances

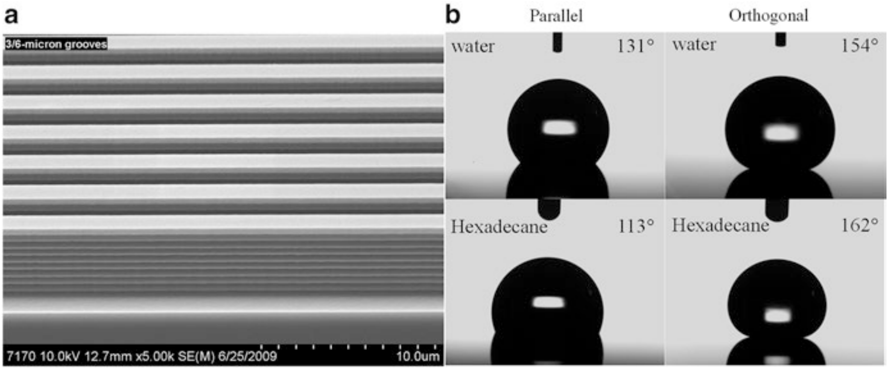

Fig. 4.35 (**a**) SEM micrographs of the groove FOTS surface and (**b**) sessile drop data of water and hexadecane on the groove FOTS surface (Reproduced with permission from [102], Copyright 2012 The American Chemical Society)

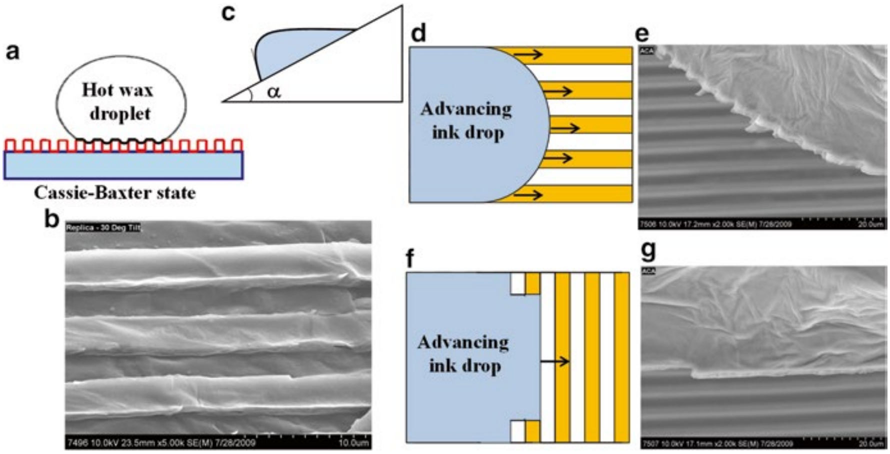

Fig. 4.36 (**a**) A schematic showing the composite interface of the hot wax drop on the groove surface, (**b**) SEM micrograph of the wax replica of the interface, (**c**) schematic of a hot wax droplet on a tilting plate, (**d**, **e**) schematic and SEM micrograph of the wax drop sliding in the parallel direction, and (**f**, **g**) schematic and SEM micrograph of the wax drop sliding in the orthogonal direction (Modified from figures in [102], Copyright 2012 The American Chemical Society)

to the next groove. This results in larger contact angle and sliding angle. In contrast, the same friction does not exist when the liquid advances in the parallel direction. The liquid simply wets the solid strip and results in smaller sliding angle and smaller contact angle. This interpretation is supported by the image of the contact lines shown and discussed below.

Similar to the pillar array surface, the composite interface between the groove surface and hydrocarbon liquid was imaged with a hot polyethylene wax droplet. The contact angles for the wax drops at 105 °C are at 156° and 120° in the orthogonal and parallel direction, respectively, indicating that the droplet is in the Cassie–Baxter state on the groove surface (Fig. 4.36a). After cooling the droplet to room temperature, the droplet was carefully detached from the groove surface. Figure 4.36b shows the SEM micrograph of the composite interface. Since the grooves are 4 µm deep, the micrograph confirms that the hot wax droplet is indeed in the Cassie–Baxter state on the groove surface. The hot wax liquid however does penetrate into the sidewall and pin underneath the re-entrant structure analogous to that of the pillar structure.

To take advantage of the hot wax experiment, Zhao and Law tilt the sessile droplet (Fig. 4.36c) in both parallel and orthogonal (Fig. 4.36d, f) directions. After liquid advances, the droplets were cooled to room temperature; the geometry of the contact lines was examined by SEM microscopy. In the parallel direction, the data show that the contact lines advance through wetting the solid strips of the groove surface, resulting in a zig-zag pattern along the contact line (Fig. 4.36e). In the orthogonal direction, liquid advance requires the contact line to "jump" from one solid strip to the next (Fig. 4.36g). Due to the high energy

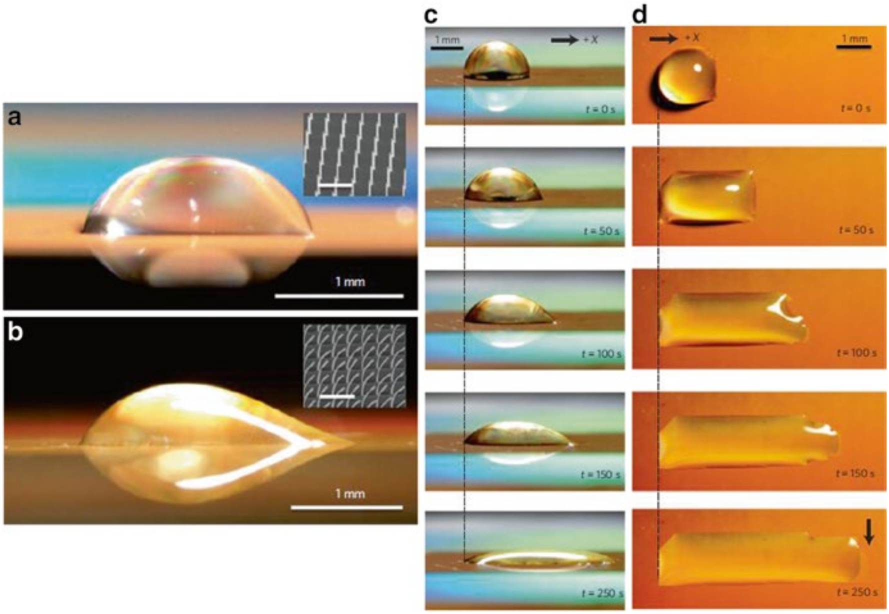

Fig. 4.37 Comparison of wetting behavior of water sessile droplets (0.002 % Triton X-100) on asymmetric nanopillar arrays with (**a**) zero and (**b**) 12° deflection [inset: SEM images of the surfaces, 10 μm scale bar]; (**c**, **d**) are time-lapse side-view and top-view images showing the spreading of a 1 μL sessile droplet on surface in b (Reproduced with permission from [103], Copyright 2010 Nature Publishing Group)

barrier in this process, the sliding angle in the perpendicular direction is larger and the contact angle is larger too due to the pinning effect.

While having a directional wetting surface is certainly interesting and may find many applications, Chu, Xiao, and Wang [103] reported recently that with a proper structural design, wetting and spreading can be unidirectional too! Using photolithographic technique, these authors first fabricated a pillar array surface with diameter ~500–750 nm, height ~10 μm, and spacing ~3.5 μm. The surface of the pillar array can be modified by a polymer coating using the CVD technique and a typical SEM image of the surface is shown in the inset of Fig. 4.37a. Pillar array surfaces with different degree of pillar deflections (from the vertical position) can be fabricated by first asymmetrically depositing a thin layer of gold on one side of the pillar using the e-beam technique, followed by coating the entire pillar structure with a CVD polymer coating. The angle of deflection is controlled by the thickness of the gold layer. Deflection angle ranges from 7° to 52° were reported and the SEM image of the surface with 12° deflection is shown in the inset of Fig. 4.37b. The water sessile drop data show that with the vertical pillar array surface, the droplet is symmetrical (Fig. 4.37a), whereas asymmetrical drop shape is observed for the surface with a 12° deflection pillar array (Fig. 4.37b). More importantly, a smaller contact angle is obtained when the advancing contact line is moving in the "with-direction" of the deflection. When the contact line is advancing against the direction of the deflection, larger contact angle is resulted. The observation is attributable to the asymmetrical friction created by the deflected pillars. This interpretation is supported when observing the spreading of the sessile drop as a function of time. Figure 4.37c, d shows the time-lapse side-view and top-view images of the sessile drop as it spreads. The photographs clearly reveal that the contact line that is against the deflected pillars (left hand side) shows no movement after the drop wets the surface. On the other hand, the contact line that is in the with-direction of the deflection moves gradually to the right, resulting in an elongated, asymmetrical droplet.

4.5 A Word About Technology Implementation

Over the last 20 years, tremendous progress has been made in understanding the fundamental principle of liquid wetting on rough surfaces. Numerous applications have been explored. The potential of combining chemistry, roughness, and roughness geometry to control and manipulate wettability, spreading, adhesion, and drop mobility appears limitless. Research activities have been diverse and rigorous. While superhydrophilicity did find applications in antifogging coating and self-cleaning surface [35], the overall implementation of the rough surface-enabled technology is still lagged when compared to the worldwide effort and investment. This is particularly true for superhydrophobicity. Many researchers have been inspired by the Lotus effect and the phenomenon seems show promises in a variety of areas. Unfortunately, most of the excitements are just hypes or simply “You Tube” moments. Large-scale adoption of any technology derived from superhydrophobicity remains elusive. There are multiple causes for this shortfall. Part of it can be attributed to the insufficient recognition of all the key parameters needed for production. Most researchers are only focused on the large contact angle and small sliding angle or low hysteresis in their technology pursue. These parameters are crucial, but they are just a starting point. Insufficient attention has been paid to key parameters such as mechanical property, oleophobicity, wetting breakthrough pressure, and manufacturability. These key parameters are essential as they are intimately tied to robustness of the product design and longevity in performance. A lot of superhydrophobic surfaces, which comprise nanoscale fine structures, are fragile mechanically. Additionally, in urban and industrial environments, exposure to volatile organics is unavoidable. If a superhydrophobic surface is contaminated by oily matter, its performance will degrade. Therefore, abrasion resistance and oleophobicity have to be considered seriously in a robust superhydrophobic product design. While the requirement for a high wetting breakthrough pressure may be a dependent of the application, manufacturing technology for large-scale and large area surface manufacturing is a must-have if mass adoption is desired. To date, very little is known about robust design parameters for manufacturing latitude and defect rate. A detailed discussion of these issues is beyond the scope of this book, but can be found in a recent chapter authored by the present authors in an upcoming book titled “Non-wettable Surfaces” edited by Ras and Marmur [104].

References

1. Wenzel RN (1936) Resistance of solid surfaces to wetting by water. Ind Eng Chem 28:988–994
2. Cassie ABD, Baxter S (1944) Wettability of porous surfaces. Trans Faraday Soc 40:546–551
3. Gao L, McCarthy TJ (2007) How Wenzel and Cassie were wrong. Langmuir 23:3762–3765
4. McHale G (2007) Cassie and Wenzel: were they really so wrong? Langmuir 23:8200–8205
5. Nosonovsky M (2007) On the range of applicability of the Wenzel and Cassie equations. Langmuir 23:9919–9920
6. Panchagnula MV, Vedantam S (2007) Comment on how Wenzel and Cassie were wrong by Gao and McCarthy. Langmuir 23:13242
7. Gao L, McCarthy TJ (2007) Reply to “Comment on how Wenzel and Cassie were wrong by Gao and McCarthy”. Langmuir 23:13243
8. Gao L, McCarthy TJ (2009) An attempt to correct the faulty intuition perpetuated by the Wenzel and Cassie “Laws”. Langmuir 25:7249–7255
9. Pease DC (1945) The significance of the contact angle in relation to the solid surface. J Phys Chem 49:107–110
10. Bartell FE, Shepard JW (1953) Surface roughness as related to hysteresis of contact angles. II. The systems of paraffin-3 molar calcium chloride solution-air and paraffin-glycerol-air. J Phys Chem 57:455–458
11. Johnson RE (1959) Conflicts between Gibbsian thermodynamics and recent treatments of interfacial energies in solid-liquid-vapor systems. J Phys Chem 63:1655–1658
12. Gray VR (1965) Surface aspects of wetting and adhesion. Chem. Ind. 969–977
13. Extrand CW (2003) Contact angles and hysteresis on surfaces with chemical heterogeneous islands. Langmuir 19:3793–3796
14. Bormashenko EA (2009) Variation approach of wetting of composite surfaces: is wetting of composite surfaces a one-dimensional or two-dimensional phenomenon? Langmuir 25: 10451–10454
15. Gao L, McCarthy TJ (2009) Wetting 101°. Langmuir 25:14105–14115
16. Meiron TS, Marmur A, Saguy IS (2004) Contact angle measurement on rough surfaces. J Colloid Interface Sci 274:637–644
17. Forsberg PSH, Priest C, Brinkmann M, Sedev R, Ralston J (2010) Contact line pinning on microstructured surfaces for liquids in the Wenzel state. Langmuir 26:860–865
18. Choi W, Tuteja A, Mabry JM, Cohen RE, McKinley GH (2009) A modified Cassie-Baxter relationship to explain contact angle hysteresis and anisotropy on non-wetting surfaces. J Colloid Interface Sci 339:208–216
19. Kanungo M, Mettu S, Law KY, Daniel S (2014) Effect of roughness geometry on wetting and dewetting of rough PDMS surfaces. Langmuir 30:7358–7368
20. Drelich J, Chibowski E (2010) Superhydrophilic and superwetting surfaces: definition and mechanisms of control. Langmuir 26:18621–18623
21. Priest C, Albrecht TWJ, Sedev R, Ralston J (2009) Asymmetric wetting hysteresis on hydrophobic microstructured surfaces. Langmuir 25:5655–5660
22. Papadopoulos P, Deng X, Mammen L, Drotlef DM, Battagliarin G, Li C, Mullen K, Landfester K, del Campo A, Butt HJ, Vollmer D (2012) Wetting on the microscale: shape of a liquid drop on a microstructured surface at different length scales. Langmuir 28:8392–8398
23. Dorrer C, Ruhe J (2006) Advancing and receding motion of droplets on ultrahydrophobic post surfaces. Langmuir 22:7652–7657
24. Hansson PM, Hormozan Y, Brandner BD, Linnros J, Claesson PM, Swerin A, Schoelkopf J, Gane PAC, Thormann E (2012) Effect of surface depressions on wetting and interactions between hydrophobic pore array surfaces. Langmuir 28:11121–11130
25. Anantharaju N, Panchagnula MV, Vedantam S, Neti S, Tatic-Lucic S (2007) Effect of three-phase contact line topology on dynamic contact angles on heterogeneous surfaces. Langmuir 23:11673–11676

26. Liu J, Mei Y, Xia R (2011) A New wetting mechanism based upon triple contact line pinning. Langmuir 27:196–200
27. Larsen ST, Taboryski RA (2009) Cassie-like Law using triple phase boundary line fractions for faceted droplets on chemically heterogeneous surfaces. Langmuir 25:1282–1284
28. Jopp J, Grll H, Yerushalmi-Rozen R (2004) Wetting behavior of water droplets on hydrophobic microtextures of comparable size. Langmuir 20:10015–10019
29. Mohammadi R, Wassink J, Amirfazli A (2004) Effect of surfactants on wetting of superhydrophobic surfaces. Langmuir 20:9657–9662
30. Wu J, Zhang M, Wang X, Li S, Wen W (2011) A simple approach for local contact angle determination on a heterogeneous surface. Langmuir 27:5705–5708
31. Cwikel D, Zhao Q, Liu C, Su X, Marmur A (2010) Comparing contact angle measurements and surface tension assessments of solid surfaces. Langmuir 26:15289–15294
32. Koch K, Bhushan B, Barthlott W (2008) Diversity of structure, morphology, and wetting of plant surfaces. Soft Matter 4:1943–1963
33. Koch K, Bhushan B, Barthlott W (2009) Multifunctional surface structure of plants. An inspiration for biomimetics. Prog Mater Sci 54:137–178
34. Hasimoto K, Irie H, Fujishima A (2005) TiO_2 photocatalysis: a historical overview and future prospect. Jpn J Appl Phys 44:8269–8285
35. Fujishima A, Zhang X, Tryk DA (2008) TiO_2 photocatalysis and related surface phenomena. Surf Sci Rep 63:515–582
36. Ogawa T, Murata N, Yamazaki S (2003) Development of antifogging mirror coated with SiO_2-ZrO_2-colloidal SiO_2 film by the Sol Gel process. J Sol-Gel Technol 27:237–238
37. Cebeci FC, Wu Z, Zhai L, Cohen RE, Rubner MF (2006) Nanoporosity driven superhydrophilicity: a means to create multifunctional antifogging coatings. Langmuir 22:2856–2862
38. Dong H, Ye P, Zhong M, Pietrasik J, Drumright R, Matyjaszewski K (2010) Superhydrophilic surfaces via polymer-SiO_2 nanocomposites. Langmuir 26:15567–15573
39. Barthlott W, Neinhuis C (1997) The purity of sacred lotus or escape from contamination in biological surfaces. Planta 202:1–8
40. Cheng YT, Rodak DE, Wong CA, Hayden CA (2006) Effects of micro and nano structures on the self-cleaning behaviour of lotus leaves. Nanotechnology 17:1359–1362
41. Ensikat EJ, Ditsche-Kuru P, Neinhuis C, Barthlott W (2011) Superhydrophobicity in perfection: the outstanding properties of the lotus leaf. Beilstein J Nanotechnol 2:152–161
42. Li W, Amirfazli A (2008) Hierarchical structures for natural superhydrophobic surfaces. Soft Matter 4:462–466
43. Liu HH, Zhang HY, Li W (2011) Thermodynamic analysis on wetting behavior of hierarchical structured superhydrophobic surfaces. Langmuir 27:6260–6267
44. Su Y, Ji B, Zhang K, Hao H, Huang Y, Hwang K (2010) Nano to micro structural hierarchy is crucial for stable superhydrophobic and water-repellent surfaces. Langmuir 26:4984–4989
45. Yu Y, Zhao ZH, Zheng QS (2007) Mechanical and superhydrophobic stabilities of two scale surfacial structure of lotus leaves. Langmuir 23:8312–8316
46. Extrand CW (2011) Repellency of the lotus leaf: resistance of water intrusion under hydrostatic pressure. Langmuir 27:6920–6925
47. Bittoun E, Marmur A (2012) The role of multi-scale roughness in the lotus effect: is it essential for superhydrophobicity. Langmuir 28:13933–13942
48. Nosonovsky M (2007) Multiscale roughness and stability of superhydrophobic biomimetic interface. Langmuir 23:3157–3161
49. Gao L, McCarthy TJ (2006) The lotus effect explained: two reasons why two length scale of topography are important. Langmuir 22:2966–2967
50. Luo C, Zheng H, Wang L, Fang H, Hu J, Fan C, Cao Y, Wang J (2010) Direct three-dimensional imaging of the buried interfaces between water and superhydrophobic surfaces. Angew Chem Int Ed 49:9145–9148
51. Cao L, Hu HH, Gao D (2007) Design and fabrication of micro-textures for inducing a superhydrophobic behavior on hydrophilic materials. Langmuir 23:4310–4314
52. Cheng YT, Rodak DE (2005) Is the lotus leaf superhydrophobic? Appl Phys Lett 85:144101

53. Boreyko JB, Chen CH (2009) Restoring superhydrophobicity of lotus leaves with vibration-induced dewetting. Phys Rev Lett 103:174502
54. Gao L, McCarthy TJ, Zhang X (2009) Wetting and superhydrophobicity. Langmuir 25:14100–14104
55. Law KY (2012) Nanostructured coatings, surfaces and film Surf Innovations 1:75–76
56. Law KY (2014) Definitions for hydrophilicity, hydrophobicity, and superhydrophobicity: getting the basics right. J Phys Chem Lett 5:686–688
57. Liu K, Jiang L (2012) Bio-inspired self-cleaning surfaces. Annu Rev Mater Res 42:231–263
58. Yan YY, Gao N, Barthlott W (2012) Mimicking nature superhydrophobic surfaces and grasping the wetting process: a review on recent progress in preparing superhydrophobic surface. Adv Colloid Interface Sci 169:80–105
59. Sas I, Gorga RE, Joines JA, Thoney KA (2012) Literature review on superhydrophobic surfaces produced by electrospinning. J Polym Sci B Polym Phys 50:824–845
60. Nishimoto S, Bhushan B (2013) Bioinspired self-cleaning surfaces with superhydrophobicity, superoleophobicity, and superhydrophilicity. RSC Advances 3:671–690
61. Celia E, Darmanin T, de Givenchy ET, Amigoni S, Guttard F (2013) Recent advances in designing superhydrophobic surfaces. J Colloid Interface Sci 402:1–18
62. Drelich J, Marmur A (2013) Physics and applications of superhydrophobic and superhydrophilic surfaces and coatings. Surf Innovations 2:211–227
63. Oner D, McCarthy TJ (2000) Ultrahydrophobic surfaces. Effect of topography length scale on wettability. Langmuir 16:7777–7782
64. Furstner R, Barthlott W, Neinhuis C, Walzel P (2005) Wetting and self-cleaning properties of artificial superhydrophobic surfaces. Langmuir 21:956–961
65. Martines E, Seunarine K, Morgan H, Gadegaard N, Wilkinson CDW, Riehle MO (2005) Superhydrophobicity and superhydrophilicity of regular nanopatterns. Nano Lett 5:2097–2103
66. Byun D, Hong J, Saputra KJH, Lee YJ, Park HC, Byun BK, Lukes JR (2009) Wetting characteristics of insect wing surfaces. J Bionic Eng 6:63–70
67. Teare DOH, Spanos CG, Ridley P, Kinmond EJ, Roucoules V, Badyal JPS, Brewes SA, Coulson S, Willis C (2002) Pulsed plasma deposition of superhydrophobic nanospheres. Chem Mater 14:4566–4571
68. Darmainbin T, Guittard F (2011) Superhydrophobic fiber mats by electrodeposition of fluorinated poly(3,4-ethyleneoxythiathiophene). J Am Chem Soc 133:15627–15634
69. Greiner A, Wendorff JH (2007) Electrospinning: a fascinating method for the preparation of ultrathin fibers. Angew Chem Int Ed 46:5670–5703
70. Ming W, Wu D, van Benthem R, de With G (2005) Superhydrophobic films from raspberry-like particles. Nano Lett 5:2298–2301
71. Ma M, Gupta M, Li Z, Zhai L, Gleason KK, Cohen RE, Rubner MF, Rutledge GC (2007) Decorated electrospun fibers exhibiting superhydrophobicity. Adv Mater 19:225–259
72. Steele A, Bayer I, Loth E (2009) Inherently superoleophobic nanocomposite coatings by spray atomization. Nano Lett 9:501–505
73. Wang J, Liu F, Chen H, Chen D (2009) Superhydrophobic behavior achieved from hydrophilic surfaces. Appl Phys Lett 95:084104
74. Feng L, Song Y, Zhai J, Liu B, Xu J, Jiang L, Zhu D (2003) Creation of a superhydrophobic surface from an amphiphilic polymer. Angew Chem Int Ed 42:800–802
75. He B, Patankar NA, Lee J (2003) Multiple equilibrium droplets shapes as design criteria for rough hydrophobic surfaces. Langmuir 19:4999–5003
76. Bico J, Marzolin C, Quere D (1999) Pearl drops. Europhys Lett 47:220–226
77. Lafuma A, Quere D (2003) Superhydrophobic states. Nat Mater 2:458–460
78. Bormashenko E, Pogreb R, Whyman G, Bormashemko Y, Erlich M (2007) Vibration-induced Cassie-Wenzel transition on rough surfaces. Appl Phys Lett 90:201917
79. Bormashenko E, Pogreb R, Whyman G, Erlich M (2007) Resonance Cassie-Wenzel wetting transition for horizontally vibrated drops deposited on a rough surface. Langmuir 23: 12217–12221
80. Liu G, Fu L, Rode AV, Craig VSJ (2011) Water droplet motion control on superhydrophobic surfaces: exploiting the Wenzel-to-Cassie transition. Langmuir 27:2595–2600

81. Xue Y, Chu S, Lv P, Duan H (2012) Importance of hierarchical structures in wetting stability on submersed superhydrophobic surfaces. Langmuir 28:9440–9450
82. Whyman G, Bormashenko E (2011) How to make the Cassie wetting state stable? Langmuir 27:8171–8176
83. Lee C, Kim CJ (2009) Maximizing the giant liquid slip on superhydrophobic microstructures by nanostructuring their sidewalls. Langmuir 25:12812–12818
84. Liu T, Sun W, Sun X, Ai H (2010) Thermodynamic analysis of the effect of hierarchical architecture of a superhydrophobic surface on a condensed drop state. Langmuir 26:14835–14841
85. Chen CH, Cai Q, Tsai C, Chen CC (2007) Dropwise condensation on superhydrophobic surfaces with two-tier roughness. Appl Phys Lett 90:173108
86. Tuteja A, Choi W, McKinley GH, Cohen RE, Rubner MF (2008) Design parameters for superhydrophobicity and superoleophobicity. MRS Bull 33:752–758
87. Tuteja A, Choi W, Mabry JM, McKinley GH, Cohen RE (2008) Omniphobic surfaces. Proc Natl Acad Sci U S A 105:18200–18205
88. Zhao H, Law KY, Sambhy V (2011) Fabrication, surface properties, and origin of superoleophobicity for a model textured surface. Langmuir 27:5927–5935
89. Tuteja A, Choi W, Ma M, Mabry JM, Mazzella SA, Rutledge GC, McKinley GH, Cohen RE (2007) Designing superoleophobic surfaces. Science 318:1618–1622
90. Choi W, Tuteja A, Chhatre S, Mabry JM, Cohen RE, McKinley GH (2009) Fabrics with tunable oleophobicity. Adv Mater 21:2190–2195
91. Fujii T, Aoki Y, Habazaki H (2011) Fabrication of super-oil-repellent dual pillar surfaces with optimized pillar intervals. Langmuir 27:11752–11756
92. Cao L, Price TP, Weiss M, Gao D (2008) Super water- and oil-repellent surfaces on intrinsically hydrophilic and oleophilic porous silicon films. Langmuir 24:1640–1643
93. Ahuja A, Taylor JD, Lifton V, Sidorenko AA, Salamon TR, Lobaton EJ, Kolodner P, Krupenkin TN (2008) Nanonails. A simple geometrical approach to electrically tunable superlyophobic surfaces. Langmuir 24:9–14
94. Kumar RTR, Mogensen KB, Boggild P (2010) Simple approach to superamphiphobic overhang nanostructures. J Phys Chem C 114:2936–2940
95. Zhao H, Park CK, Law KY (2012) Effect of surface texturing on superoleophobicity, contact angle hysteresis, and "robustness". Langmuir 28:14925–14934
96. Zheng Y, Gao X, Jiang L (2007) Directional adhesion of superhydrophobic butterfly wing. Soft Matter 3:178–182
97. Wu D, Wang JN, Wu SZ, Chen QD, Zhao S, Zhang H, Sun HB, Jiang L (2011) Three-level biomimetic rice-leaf surfaces with controllable anisotropic sliding. Adv Funct Mater 21:2927–2932
98. Yoshimitsue Z, Nakajima A, Watanabe T, Hashimoto K (2002) Effects of surface structure on the hydrophobicity and sliding behavior of water droplets. Langmuir 18:5818–5822
99. Xia D, Brueck SRJ (2008) Strongly anisotropic wetting on one-dimensional nanopatterned surfaces. Nano Lett 8:2819–2824
100. Xia D, He X, Jiang YB, Lopez GP, Brueck SRJ (2010) Tailoring anisotropic wetting properties on submicrometer-scale periodic grooved surfaces. Langmuir 26:2700–2706
101. Yang J, Rose FRA, Gadegaard N, Alexander MR (2009) Effect of sessile drop volume on wetting anisotropy observed on grooved surfaces. Langmuir 25:2567–2571
102. Zhao H, Law KY (2012) Directional self-cleaning superoleophobic surfaces. Langmuir 28: 11812–11818
103. Chu KH, Xiao R, Wang EN (2010) Uni-directional liquid spreading on asymmetric nanostructured surfaces. Nat Mater 9:413–417
104. Law KY, Zhao H (2015) Design principles for robust superoleophobicity and superhydrophobicity. In Ras R, Marmur A (eds) Non-wettable surfaces, Royal Society of Chemistry, to be published.